



HAL
open science

Geodynamic evolution of the Tethyan lithosphere as recorded in the Spontang Ophiolite, South Ladakh ophiolites (NW Himalaya, India)

Mallika Jonnalagadda, Mathieu Benoit, Shivani Harshe, Romain Tilhac, Raymond Duraiswami, Michel Grégoire, Nitin Karmalkar

► **To cite this version:**

Mallika Jonnalagadda, Mathieu Benoit, Shivani Harshe, Romain Tilhac, Raymond Duraiswami, et al.. Geodynamic evolution of the Tethyan lithosphere as recorded in the Spontang Ophiolite, South Ladakh ophiolites (NW Himalaya, India). *Geoscience Frontiers*, 2022, 13 (1), pp.101297. 10.1016/j.gsf.2021.101297 . hal-03378242

HAL Id: hal-03378242

<https://hal.science/hal-03378242>

Submitted on 20 Oct 2021

HAL is a multi-disciplinary open access archive for the deposit and dissemination of scientific research documents, whether they are published or not. The documents may come from teaching and research institutions in France or abroad, or from public or private research centers.

L'archive ouverte pluridisciplinaire **HAL**, est destinée au dépôt et à la diffusion de documents scientifiques de niveau recherche, publiés ou non, émanant des établissements d'enseignement et de recherche français ou étrangers, des laboratoires publics ou privés.

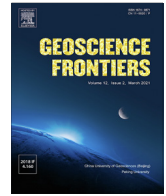


Distributed under a Creative Commons Attribution 4.0 International License



Contents lists available at ScienceDirect

Geoscience Frontiers

journal homepage: www.elsevier.com/locate/gsf

Research Paper

Geodynamic evolution of the Tethyan lithosphere as recorded in the Spontang Ophiolite, South Ladakh ophiolites (NW Himalaya, India)



Mallika K. Jonnalagadda^{a,b,c,*}, Mathieu Benoit^c, Shivani Harshe^b, Romain Tilhac^d,
Raymond A. Duraiswami^b, Michel Grégoire^c, Nitin R. Karmalkar^{b,e}

^a Interdisciplinary School of Science, Savitribai Phule Pune University, Pune 411007, India

^b Department of Geology, Savitribai Phule Pune University, Pune 411007, India

^c Géosciences Environnement Toulouse, CNRS-CNES-IRD-Université Paul Sabatier, Observatoire Midi Pyrénées, 31400 Toulouse, France

^d Instituto Andaluz de Ciencias de la Tierra (IACT), CSIC – Universidad de Granada, 18100 Armilla, Granada, Spain

^e Vice-Chancellor's Office, Savitribai Phule Pune University, Pune 411007, India

ARTICLE INFO

Article history:

Received 17 October 2020

Revised 22 March 2021

Accepted 12 September 2021

Available online 13 September 2021

Handling Editor: S.Z. Li

Keywords:

Peridotites

Mafic rocks

Partial melting

Metasomatism

Ladakh

ABSTRACT

The Spontang Ophiolite complex represents the most complete ophiolite sequence amongst the South Ladakh ophiolites and comprises mantle rocks (depleted harzburgites, dunites and minor lherzolites) as well as crustal rocks (basalt, isotropic gabbros, layered gabbros etc.). In the present study, detailed geochemistry (whole rock as well as mineral chemistry) and Sr-Nd isotopic analyses of thirty-six ultramafic-mafic samples have been attempted to constraint the evolution and petrogenetic history of the Tethyan oceanic crust. Major, trace-element and REE patterns of the peridotites and their minerals indicate that the lherzolites experienced lower degrees of partial melting resembling abyssal peridotites (at higher temperatures, $T_{\text{REE}} = \sim 1216$ °C) than the harzburgites (6%–8% versus 15%–17%). Elevated $\varepsilon_{\text{Nd}}(t)$ and variable $^{87}\text{Sr}/^{86}\text{Sr}(t)$ ratios along with REE patterns suggest that the Spontang mafic rocks display N-MORB affinity with negligible participation of oceanic sediments in their genesis are originated from a depleted upper mantle with little contribution from subduction-related fluids. MORB-type Neotethyan oceanic crust is associated with the earliest phase of subduction (of older Jurassic age) through which a younger intra-oceanic island arc (Spong arc) subsequently developed. Harzburgites REE display typical U-shaped patterns, suggesting that these rocks have been metasomatized by LREE-enriched fluids. On the other side, mafic rocks are characterized by heterogeneous $(\text{Nb}/\text{La})_{\text{PM}}$ and $(\text{Hf}/\text{Sm})_{\text{PM}}$ and relatively homogeneous $\varepsilon_{\text{Nd}}(t)$, indicating interaction of subduction-related melts with the upper mantle during the initiation of subduction, in Early Cretaceous times.

© 2021 China University of Geosciences (Beijing) and Peking University. Production and hosting by Elsevier B.V. This is an open access article under the CC BY-NC-ND license (<http://creativecommons.org/licenses/by-nc-nd/4.0/>).

1. Introduction

Ophiolites are the remnants of fossil oceanic lithosphere that have been tectonically emplaced on continental margins and are considered key to reconstruct the magmatic and tectonic history of the oceanic lithosphere (Dilek and Furnes, 2011). Ophiolites depict fragments of upper mantle and oceanic crust (Dewey and Bird, 1971; Coleman, 1977; Nicolas, 1989) integrated into continental margins during continent–continent and arc–continent collisions (Dick and Flower, 2003), ridge–trench interactions (Cloos, 1993; Lagabrielle et al., 2000), and/or subduction–accretion

occurrences (Cawood et al., 2009). Ophiolites although dismembered, compared to mantle xenoliths which are volumetrically smaller in number and in size, offer a unique opportunity to study the relationships within and between the mantle and crustal units. Systematic studies using sophisticated instrumentation have made determination of geochronological, geochemical and isotopic characteristics of both crustal and mantle units of ophiolites possible. Specifically, geochemical and isotopic studies of mantle peridotites and crustal rocks from oceanic floor and ophiolitic type settings are important to characterize the chemical and isotopic heterogeneity of the mantle (Zindler and Hart, 1986). Detailed geochemical studies of mantle peridotites from ophiolitic suites provide important information on melting processes, melt extraction episodes and interaction of oceanic crust, mantle melts and fluids in the paleo-oceanic lithosphere–asthenosphere system under active tectonic

* Corresponding author at: Interdisciplinary School of Science, Savitribai Phule Pune University, Ganeshkhind, Pune 411007, India.

E-mail address: jmallika@gmail.com (M.K. Jonnalagadda).

conditions (Kelemen et al., 1992; Barth et al., 2003; Dilek et al., 2007; Ishikawa et al., 2007). Geochemical studies of these ancient oceanic lithospheric terranes are therefore important in order to constrain the magmatic processes involved in oceanic crust genesis, i.e. partial melting, fractional crystallization and melt/fluid-rock reactions (Shervais, 2001; Pearce, 2003; Aldanmaz et al., 2008).

The Tethyan Ophiolitic Belt formed as a consequence of the closure of the Tethyan Ocean and collision of the Indian and Eurasian tectonic plates (Pal et al., 2003; Ghosh et al., 2017) and are marked by several events such as the subduction of the Indian plate beneath Eurasia, ophiolite obduction onto the continental margin, high pressure – low temperature metamorphism and collision-accretion activities (Dilek et al., 1999; Robertson 2000; Aldanmaz et al., 2008). The Tethyan ophiolites stretching from western Europe to India and China represent multiple suture zones within the Alpine, Mediterranean and Himalayan-Tibetan orogenic belts. Several ophiolitic slivers are exposed in several locations from Spain through the Alps, Turkey, Iran, Oman, Pakistan, India, Tibet, Burma and Indonesia (Saha, 2010). Departing from the original 1972 Penrose definition (Anonymous, 1972), numerous studies on the Tethyan ophiolites have significantly improve our understanding of both ophiolites and oceanic crust, in general. The Tethyan orogenic belt preserve ophiolitic slivers in two tectonic settings viz. within the suture zone (e.g. Xigase ophiolite, south Tibet; Nicolas et al., 1981; Göpel et al., 1984) and those obducted onto the passive continental margin (e.g. Oman ophiolite; Lippard, 1986). Considering the expanse of the Himalayas and the distance the Indus suture runs, few ophiolite complexes are observed within the Himalayan belt (Fig. 1), mainly because they form the highest structural thrust sheet and more often than not, they are subjected to intense erosion. The Spontang ophiolite complex located south of the Indus Suture Zone (Fuchs, 1979; Reuber, 1986; Searle, 1986) forms the highest level of the allochthon above the marine sediments of the Lamayuru accretionary complex. In this study, we present petrology and whole rock (major- and trace-element and Sr/Nd isotopic) geochemical compositions of

both mafic and ultramafic rocks along with mineral chemistry (major and REE) of the ultramafic minerals with a view to evaluate their petrogenesis and geodynamic implications.

2. Geological setting

The Indus Tsangpo Suture Zone (ITSZ) is a significant crustal lineation representing the collisional boundary between the continental plates of Southern India and Northern Eurasia (Le Fort, 1975; Molnar and Tapponnier, 1975; Gansser, 1977). It is regarded to depict the remnants of Neo-Tethys ocean sandwiched between the Karakoram zone in the north and the Zaskar zone of the Tethys Himalayas in the south (Gansser, 1980; Srikantia and Razdan, 1981). Remnants of this Neo-Tethyan ocean are preserved along the suture as ophiolitic slivers in the Ladakh area (Gansser, 1977; Srikantia and Razdan, 1981; Honegger et al., 1982; Robertson, 2000; Maheo et al., 2004; Ahmad et al., 2008) with cor-relatives found in the east in Tibet (Nicolas et al., 1981; Girardeau et al., 1985a, b; Zhou et al., 1998; Aitchison et al., 2000; McDermid et al., 2002; Miller et al., 2003; Xia et al., 2003; Dubois-Côté et al., 2005; Dupuis et al., 2005; Aitchison et al., 2007; Bédard et al., 2009) and the west in Pakistan (Jan et al., 1985; Sarwar, 1992; Zaigham and Mallick, 2000; Kakar et al., 2013a, b).

The Ladakh ophiolites are arranged in an east–west direction and divided into the North and South Ladakh group of ophiolites based on their geographic position (Maheo et al., 2004). The South Ladakh ophiolites consists of the Spontang massif which is the most complete fragments of the Neo Tethys ocean to be preserved along the ITSZ (Fuchs, 1982; Reuber, 1986; Searle, 1986). The Nidar ophiolite (~140 Ma) located about 120 km west is the closest nearly complete ophiolite series to the Spontang Massif (Maheo et al., 2004; Ahmad et al., 2008; Zybrev et al., 2008) whereas the Karzok ophiolitic slice is considered to be detached klippe of Nidar ophiolite (de Sigoyer et al., 1997). The northern Ladakh alpine ophiolite group is preserved as extremely deformed and dismembered discrete slices best exposed in the Dras and Suru valleys (Gansser, 1980; Srikantia and Razdan, 1981; Honegger et al., 1982;

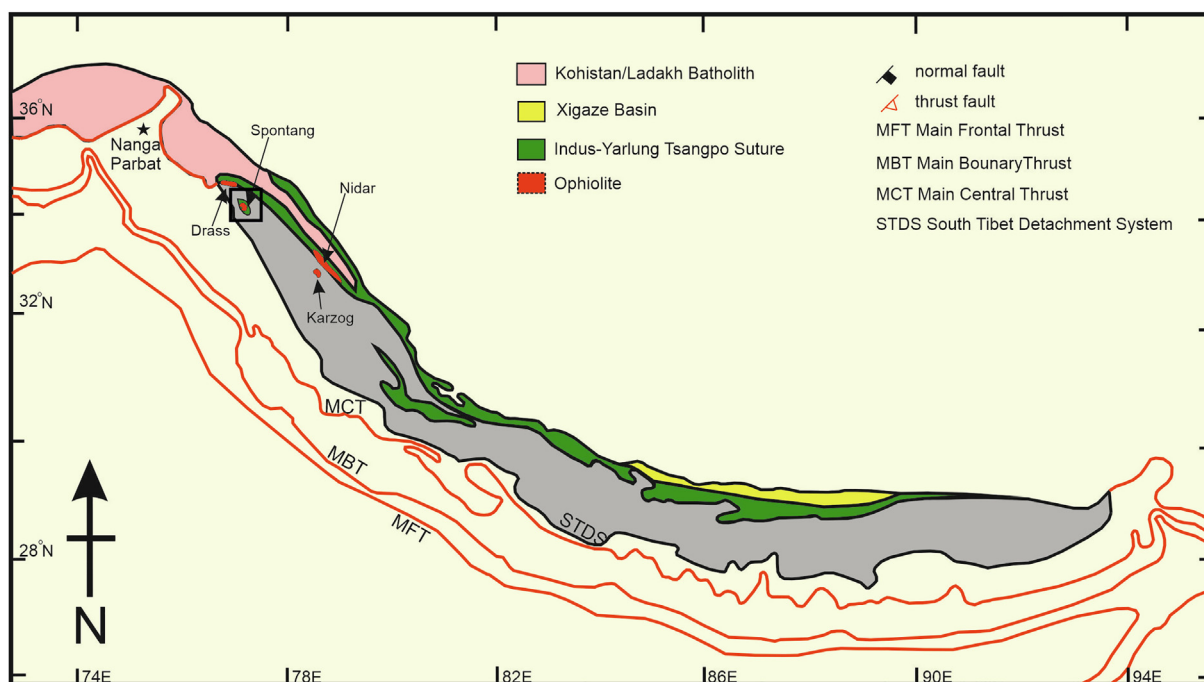


Fig. 1. Regional geological map of the Himalayas (after Hébart et al., 2003) showing location of the South Ladakh (Spontang, Nidar and Karzok) and North Ladakh ophiolite (Drass) sequences of Maheo et al. (2004). The study area has been demarcated by a box.

Radhakrishna et al., 1984; 1987; Reuber et al., 1989; Sinha and Mishra, 1994; Robertson, 2000).

The Spontang massif located 30 kms south of the Indus Suture Zone (Fuchs, 1979; Reuber, 1986; Searle, 1986) is exposed near the village of Photoksar with elevations ranging between 4000 and 6000 m (Fig. 2). Forming part of the South Ladakh group of ophiolites (after Maheo et al., 2004), the Spontang ophiolite displays most elements of a complete ophiolite sequence as defined by the Penrose-style stratigraphic sequence (Anonymous, 1972). The area has been a major attraction to many geologists who are credited with provided detailed geological maps as a result of several expeditions (Fuchs, 1979, Honegger et al., 1982; Reibel and Reuber, 1982; Bassoulet et al., 1983; Keleman and Sonnenfeld, 1983; Colchen and Reuber, 1986; Colchen et al., 1987; Reuber, 1986; Reuber et al., 1989; Reuber et al., 1992; Corfield et al., 2001). The Spontang Ophiolite can be subdivided into a western mantle unit (Reuber et al., 1986; Corfield et al., 2001) and an eastern crustal unit (Corfield et al., 1999; 2001; Pedersen et al., 2001) with much of the sequence being tectonically disturbed by faulting and the maximum exposed vertical thickness of the deformed ophiolite of 1 km (Corfield et al., 1999). The complete ophiolite sequence is significantly dismembered by deformation. The Spontang ophiolite consists of an upper mantle depleted harzburgites and dunites (Reuber et al., 1989) and some lower crustal cumulates (Reibel and Reuber, 1982; Reuber, 1986) along with gabbros, sheeted dykes and pillow lavas (Corfield and Searle, 2000) (Fig. 2a). Under the Spontang ophiolite, the Photang Thrust sheet (Corfield et al., 1999) consists of tectonic mixtures and volcanic units connected with marine sediments. Detailed field relationships between mantle and crustal units have been presented in Jonnalagadda et al. (2019) and are summarized below for ready reference.

Approximately 5 km west of Photoksar village along the Phu River, an extensive sequence of crustal rocks composed of high level gabbros and pillow lavas is exposed along the eastern flank of the Photang Valley at base of the massive Photang Kangri. A gradational contact of the sheeted dykes (Fig. 2b) with the overlying pillow lavas is observed downstream in the eastern side of the Photang valley (Fig. 2c). Some exposures reveal characteristic basalt – basalt and gabbro – basalt intrusive relationships. Isotropic gabbros were identified at the base of the dyke sequence with absence of massive and layered varieties.

The N-S ridge separating the Photang and Spong valleys, reaches over 5500 m and exposes an excellent structural section through the Photang Thrust Sheet. The mantle sequences exposed in the Spong valley consisting of depleted harzburgites (Fig. 2d) overlain by an upper lherzolitic unit are well exposed in the high cliffs of the upper Spong valley and near the upper peaks of Sisir La. Dunitic bodies are commonly observed either as large boulders (Fig. 2e, f) or intruding the peridotite units. Several gabbroic and trondhjemitic dykes are seen to crosscut the mantle units (Fig. 2g), some several meters in width consistent with earlier reports by Corfield et al. (2001).

Lower crustal sequences viz. weathered cumulates of wehrlites and pyroxenites (Fig. 2h) with associated gabbros are exposed in the Marling Chu valley and the Bumiktse valleys. The highly tectonized gabbros in the Bumiktse valley are exposed below the snout of the glacier and are thrust directly onto the volcano-sedimentary sequence of the lower Bumiktse Valley. Crustal sections exposed along both valleys and west of Bumiktse are observed to continue across the inaccessible vertical cliffs and glaciers of the Photang Kangri. South of the Photoksar village, a gradational transition of ophiolitic units to a volcano-sedimentary sequence of pillow lavas and interbedded volcanoclastic deposits on the northern edge of the Photang Kangri and along the Bumiktse and Marling valleys is observed (Fig. 2i). These volcanic

and volcanoclastic sequences of island-arc affinity (Spong arc) which tectonically overly the Spontang ophiolite are believed to be associated with an immature array of the island forming above the oceanic substratum of the Spontang ophiolite (Reuber et al., 1992; Corfield et al., 2001). There is no clearly defined contact between the units; however, depending on the start of volcanoclastic deposits in the field, a transition can be noted. The sequence of several 100 m thick units, consisting of angular and poorly sorted clasts, is widely displayed in the Bumiktse valley with occasional clasts of chert.

3. Samples and petrography

A total of thirty-six samples consisting of ultramafic and mafic rocks were analyzed in the present study (Table 1). The mafic samples are represented by basaltic dyke intrusions into the peridotites and gabbros whereas the ultramafic rocks comprise depleted harzburgites, minor lherzolites and dunites. Detailed petrography of the peridotite samples is presented in Jonnalagadda et al. (2019) and summarized below for ready reference.

Harzburgites are coarse-grained and display porphyroclastic to protogranular textures. Their primary modal mineralogy includes olivine (60 to 75 vol.%), orthopyroxene (15 to 30 vol.%), minor clinopyroxene relics (<1 vol.%) with accessory spinel (less than 3 vol%). Olivines are coarse, exhibit undulose extinction surrounded by smaller crystals of olivine and display curvilinear boundaries meeting at triple junctions. Zoning, kink bands, and recrystallization are commonly observed (Fig. 3a). Orthopyroxenes are colorless, generally occurring as big prismatic crystals, 0.2 to 3.5 mm in size with curvilinear boundaries and often showing exsolution lamellae, kink bands and gliding (Fig. 3b, c). Minor clinopyroxenes are interstitial, 0.1 to 0.3 mm in length and show pale green color in polarized air light with sutured boundaries.

Lherzolite specimens demonstrate textural shift from porphyroclastic to equigranular mosaic texture. Feeble alteration to serpentine is observed at places. Subhedral olivine occurs as porphyroclasts (0.3 to 1.5 mm) whereas anhedral grains are observed as mosaic crystals with curved boundaries. Both generations show curvilinear, serrated boundaries, recrystallization, and the presence of kink bands (Fig. 3d). Clinopyroxene may be present in the olivine matrix as porphyroclasts with exsolution lamellae of orthopyroxenes (Fig. 3e). Spinel exsolution lamellae are noted in the orthopyroxenes at places.

Dunites are fresh, unaltered, with granular texture. Coarse olivine grains are large, porphyroclastic, elongated and display undulose extinction and intense zoning (Fig. 3f). They range in size from 0.9 to 4.00 mm and are surrounded by smaller subhedral grains. Matrix olivines are subhedral to anhedral 0.5 to 2 mm in size and display polygonization and serrated boundaries. Euhedral spinels are commonly observed along olivine boundaries or as inclusions within olivines.

Gabbros are medium- to fine-grained foliated rocks displaying inequigranular to protomylonitic texture and predominantly contain hornblende, relic pyroxenes and plagioclase phenocrysts, Fe-Ti oxides and secondary minerals such as epidote and quartz. Plagioclase crystals are elongate and cloudy with anorthositic core and albitized rims (Fig. 3g). They rarely show polysynthetic twinning. Pyroxenes are augitic in composition ($En_{0.26-0.36}Fs_{0.38-0.55}Wo_{0.08-0.28}$) and occur as relict anhedral grains with two distinct set of cleavages at right angles to each other and display simple twinning. In most samples, the pyroxenes are completely altered to amphiboles with greenish magnesio-hornblende core and brownish Ti-rich magnesio-hornblende rims. The gabbros are affected to low degrees of sea-floor metamorphism as observed

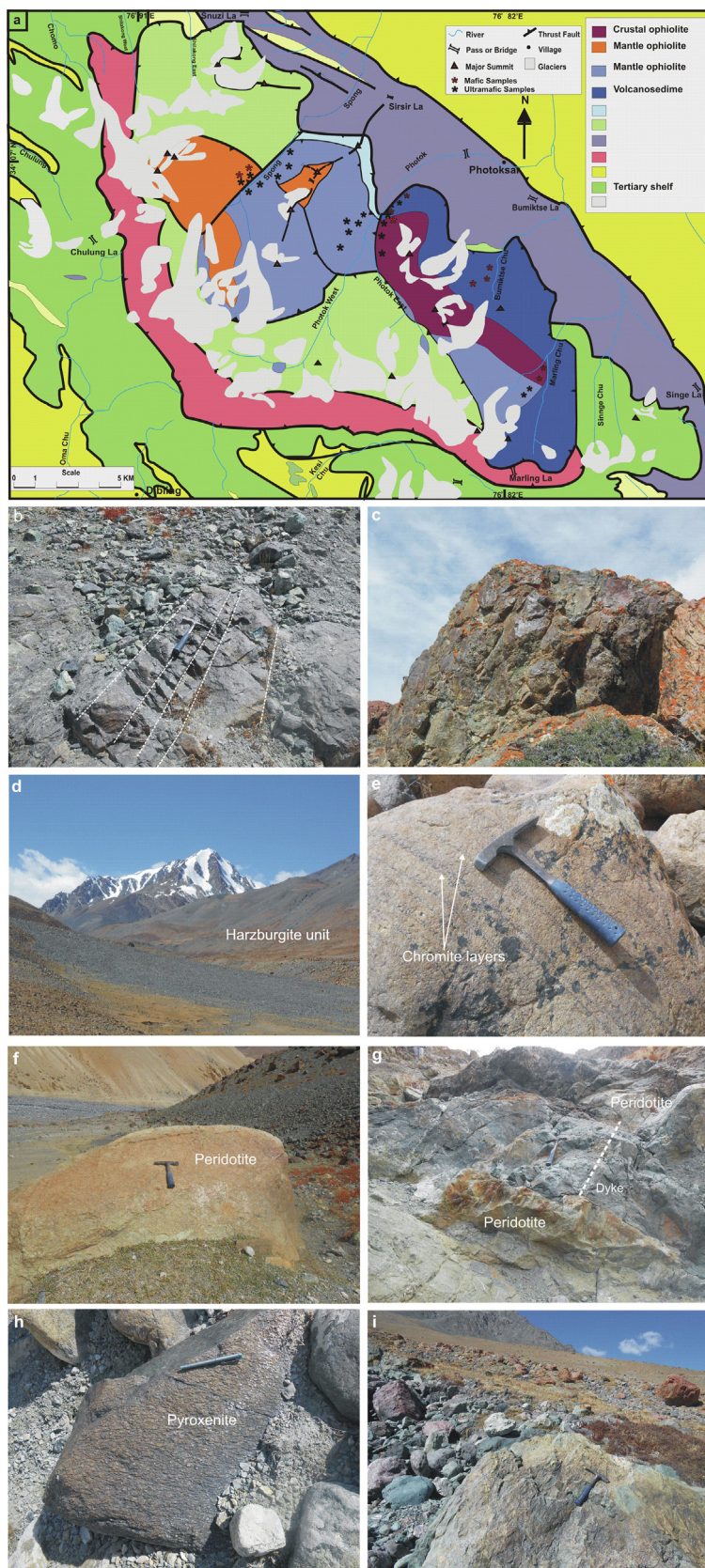


Fig. 2. (a) Detailed geological map of the Spontang ophiolite showing the major tectonic units (after Corfield et al., 2001). Red and black stars indicate sample locations of the mafic and ultramafic samples respectively. (b) Contact of the sheeted dykes with the overlying pillow lavas as observed downstream in the eastern side of the Photang valley. (c) Outcrops of pillow lavas exposed in the western side of the Photang Valley. (d) Harzburgite unit exposed in the upper Spong valley near the upper peaks of Sisir La. (e) Chromite layering visible in boulders of Dunite. (f) Boulders of peridotite (dunite) exposed in the upper Spong valley. (g) Mafic dykes are observed intruding the mantle units with sharp boundaries. (h) Boulders of pyroxenites exposed in the Marling Chu valleys. (i) Volcano-sedimentary sequence of pillow lavas and interbedded volcanoclastic deposits exposed in the Bumiktse valley.

Table 1

Summary of location as well as the coordinates of ultramafic and mafic samples of the Spontang ophiolite complex.

Sr. No.	Location	Sample No.	Abbreviation Used	Rock Type	Latitude	Longitude	Altitude (m)
1	Photok valley	MAR/1/PB	A1	Basalt	34° 04.419'	76°47.991'	4277
2		MAR/2/PB	A2	Basalt	34° 04.398'	76°47.940'	4285
3		SH/1/P	B1	Harburgite	–	–	–
4		SH/2/D	B2	Lherzolite	34°06.756'	76°46.512'	4512
5		SH/3/G	B3	Gabbro	–	–	–
6		SH/4/P	B4	Harburgite	–	–	–
7		SH/5/G	B5	Gabbro	–	–	–
8		SH/6/H	B6	Harburgite	–	–	–
9		SH/8/G	B8	Gabbro	34°06.670'	76°46.380'	4564
10		SH/10/P	B10	Lherzolite	–	–	–
11		SH/12/G	B12	Gabbro	34°07.412'	76°46.812'	4455
12		ST/3/G	B15	Gabbro	–	–	–
13		St/4/D	B16	Harburgite	34°07.412'	76°46.812'	4455
14	Marling Valley	MAR2/8/P	C8	Harburgite	34°04.013'	76°47.082'	4394
15		MAR2/9/P	C9	Lherzolite	34°04.013'	76°47.082'	4394
16		MAR2/10/G	C10	Gabbro	34°03.943'	76°46.997'	4416
17	Western Side of Photok Valley	SH2/2/P	D2	Harburgite	34°07.103'	76°46.575'	4519
18		SH2/5/P	D5	Harburgite	34°06.990'	76°46.500'	4534
19		UR/5/P	D11	Lherzolite	34°03.940'	76°46.828'	4463
20		UR/8/G	D14	Gabbro	34°03.940'	76°46.828'	4463
21	Spontang valley	SPO/1/P	E1	Harburgite	34°06.591'	76°46.645'	4526
22		SPO/2/G	E2	Gabbro	34°06.445'	76°46.314'	4587
23		SPO/4/H	E4	Harburgite	34°06.190'	76°46.044'	4636
24		SPO/5/D	E5	Dunite	34°06.143'	76°45.994'	4640
25		SPO/7/D	E7	Harburgite	–	–	–
26	Western Marling Valley	PYX 1/16	G1	Dunite	34°00.546'	76°52.300'	4338
27		PYX 2/16	G2	Harburgite	34°00.530'	76°52.379'	4335
28		G 3/16	G7	Harburgite	34°00.348'	76°51.954'	4404
29		PD 2/16	G6	Harburgite	34°00.368'	76°51.500'	4465
30	Spong Valley	PDT/SPO/16	I1	Harburgite	34°06.470'	76°46.542'	4581
31		PYX3/SPO/16	I4	Lherzolite	34°06.158'	76°46.285'	4615
32		G2/SPO/16	I6	Gabbro	–	–	–
33		HZ/SPO/16	I7	Harburgite	34°06.210'	76°46.328'	4607
34	D/SPO/16	I8	Harburgite	34°05.946'	76°46.010'	4630	
35	Bhumiktse valley	B/BHU/16	J3	Basalt	–	–	–
36	From Photoksar to Wanla - Sisir La pass	SP3/15/14	SP3	Dunite	34° 06. 410'	76° 46.766'	4654

by albitization of feldspars, uralitization of pyroxenes and presence of secondary epidote and quartz (Fig. 3h).

4. Analytical methods

4.1. Whole-rock analyses

Whole rock major- and trace-element data are presented in [Supplementary Data, Table S1](#). Whole-rock major-element analyses were obtained by X-ray fluorescence (XRF) on fusion glass disks using a Bruker S4 Pioneer model wavelength dispersive X-ray spectrometer at the National Centre for Earth Science Studies (NCESS), Kerala. The sample preparation method was carried out using a Katanax X-300 X-Fluxer triple station fusion instrument using standard procedures in the sample preparation lab of NCESS. Reliable and international calibration standards were used during the analysis. The analytical uncertainty is estimated to be $\pm 1\%$ for all major oxides.

Trace elements, including rare earth elements (REE), were analyzed following detailed sample preparation and analytical procedures described by [Barrat et al. \(2007\)](#). For the mafic samples, about 100 mg of whole-rock powder was accurately weighed and transferred to 22 ml Savillex PFA beakers. An amount (between 1.5 and 15 ng) of Tm (in solution) was added to each sample, except to the blank and to the reference material BHVO-2. The sample was dissolved in a mixture 1:1 HF/HNO₃. After total dissolution, samples were treated with 5 ml 2% HNO₃ and aliquots were taken, diluted and their concentrations determined with an

ELEMENT XR, Thermo-Scientific inductively coupled plasma mass spectrometer (ICP-MS) following [Barrat et al. \(2007\)](#) protocols. The ⁸⁷Rb/⁸⁶Sr and ¹⁴⁷Sm/¹⁴⁴Nd ratios were specifically monitored and international geostandards BEN, UBN and blanks were regularly run during the set. Analytical procedures for ultramafic samples have been elaborated in [Jonnalagadda et al. \(2019\)](#).

Whole-rock Sr- and Nd-isotope compositions for 12 mafic and solely Sr compositions for 14 peridotite samples were analyzed ([Table 2](#)) in the isotope laboratory at Geoscience Environment Toulouse laboratory-OMP, Toulouse France using a TRITON + Thermo-Scientific mass spectrometer (TIMS), following procedures described by [Muñoz et al. \(2018\)](#). Sr and Nd have been separated and purified by column chromatography from an aliquot of the solution taken after sample digestion for trace-element determination using a combination of Sr-Spec, Thru-spec and Ln-Spec resins. An equivalent of 250 ng Sr and 100 ng Nd were measured together with NBS987 and La Jolla isotopic standards. Standard analyses yielded 0.510848 ± 6 (n = 50) for La Jolla and 0.710255 ± 20 (n = 70) for NBS-987 which fall within the GeoRem recommended values (<http://georem.mpch-mainz.gwdg.de/>). Typical blanks are 20 pg for Nd and 150 pg for Sr. ⁸⁷Sr/⁸⁶Sr and ¹⁴³Nd/¹⁴⁴Nd ratios were normalized against ⁸⁶Sr/⁸⁸Sr = 0.1194 and ¹⁴⁶Nd/¹⁴⁴Nd = 0.7219.

4.2. Mineral chemistry

Representative mineral compositions of olivine, pyroxenes, and spinel from the investigated samples are given in [Supplementary](#)

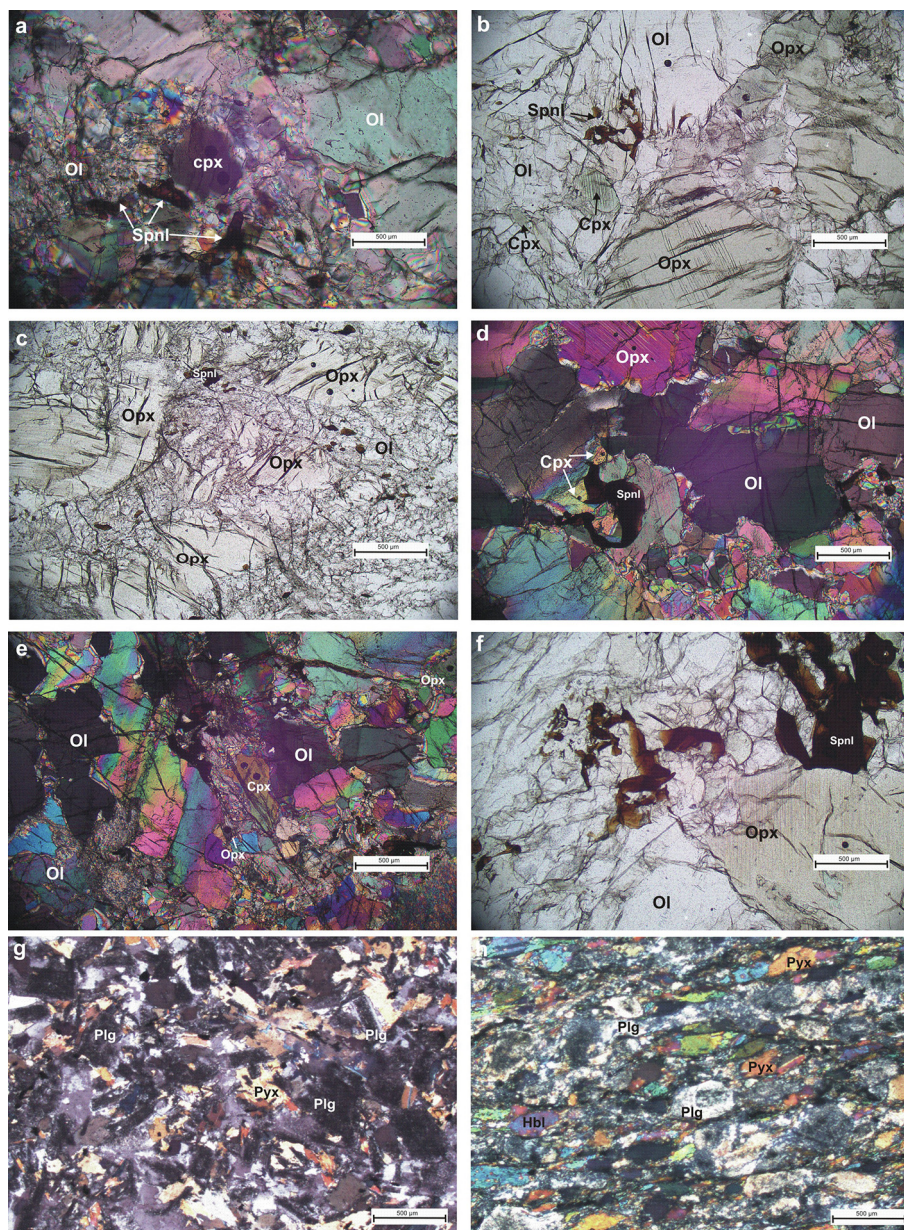


Fig. 3. Microphotographs of the ultramafic and mafic rocks of the Spontang ophiolite complex. (a) Olivines displaying curvilinear boundaries displaying zoning, kink bands, and recrystallization in the harzburgites. (b) and (c) Colorless orthopyroxenes occurring as big prismatic crystals displaying exsolution lamellae, kink bands and gliding. (d) Porphyroclasts of olivine show curvilinear, serrated boundaries, with the presence of kink bands in the lherzolites (e) Interstitial clinopyroxene observed in the matrix displaying exsolution lamellae of orthopyroxenes. (f) Dunites exhibiting coarse porphyroclastic olivine grains that are elongated and display undulose extinction and intense zoning. Anhedral spinels are commonly observed along olivine boundaries. (g) Elongate plagioclase crystals with a cloudy appearance along with relic pyroxenes Fe-Ti oxides observed in the gabbros. (h) Alteration of feldspars, pyroxenes and presence of secondary epidote and quartz observed in the gabbros.

Data, Table S2. Major-element analyses of minerals were performed with an CAMECA SX-Five electron microprobe at the Centre de Micro-caractérisation Raimond Castaing UMS-CNRS 3623, Paul Sabatier University (Toulouse). The operating conditions were set at 15 kV with 20 or 10 nA beam currents. Natural minerals and synthetic pure oxides were used as reference materials. The electron microprobe used in this study had one energy dispersive and five-wavelength dispersive spectrometers capable of automated quantitative analysis.

Trace-element including REE concentrations of clinopyroxene, orthopyroxene and olivine were determined by laser ablation (LA)-ICP-MS via a NWR213 Laser Ablation system coupled to a Thermo ELEMENT XR ICP-MS system at Geoscience Environment

Toulouse laboratory-OMP, Toulouse, France (Supplementary Data, Table S3). The reference materials used as external standards were synthetic calcium-sodium aluminosilicate glass with a concentration of approximately 400 ppm (NIST 610) and 40 ppm (NIST 612) for a wide range of trace elements. Ca concentrations determined by electron microprobe were used as an internal standard for clinopyroxene analyses. The laser-spot diameter ranged from 30 to 50 μm , with a frequency of 10 Hz, and the fluence ranged from 5 to 10 $\text{J}\cdot\text{cm}^{-2}$ (energy density). The Glitter 4.0 software (Van Achterbergh et al., 2001) was used for raw data processing. Detection limits for most elements are in the range of 10 to 60 ppb except for Sc and V (100 ppb) and Ti (2 ppm), Ni and Cr (0.7 ppm).

Table 2
Rb-Sr and Sm-Nd isotopic compositions of the mafic and ultramafic rocks of the Spontang ophiolite complex.

Sample No	A2	A1	J3	B8	B3	E2	D14	C10	B15	B5	B12	I6
Rock Type	Basalt	Basalt	Basalt	Gabbro								
⁸⁷ Rb/ ⁸⁶ Sr ICPMS	0.007	0.104	0.035	0.23	0.040	0.22	0.044	0.022	0.060	0.005	0.038	0.034
⁸⁷ Sr/ ⁸⁶ Sr measured	0.708943	0.704243	0.704863	0.705166	0.705121	0.704918	0.703795	0.703746	0.703792	0.705795	0.703703	0.70409
error: 10–6	5	5	5	4	4	5	4	5	5	5	5	5
¹⁴⁷ Sm/ ¹⁴⁴ Nd ICPMS	0.216	0.198	0.201	0.208	0.217	0.209	0.206	0.217	0.213	0.223	0.224	0.204004
⁸⁷ Sr/ ⁸⁶ Sr age corrected	0.708924	0.703982	0.704775	0.704599	0.705020	0.704366	0.703684	0.703690	0.703641	0.705784	0.703608	0.704004
¹⁴³ Nd/ ¹⁴⁴ Nd measured	0.513014	0.513040	0.513099	0.513087	0.513028	0.513042	0.513044	0.51304	0.513054	0.513085	0.513039	0.513040
error: 10–6	3	3	5	20	11	3	4	5	5	4	5	9
Ages (Ma)	177	177	177	177	177	177	177	177	177	177	177	177
¹⁴³ Nd/ ¹⁴⁴ Nd age corrected	0.512764	0.512811	0.512866	0.512846	0.512777	0.512800	0.512806	0.512788	0.512808	0.512826	0.512779	0.512801
eNd(t)	6.9	7.8	8.3	8.5	7.2	7.6	7.7	7.4	7.8	8.1	7.2	7.1
Sample No	C8	B4	E7	B16	D2	B1	D5	E4	B10	B2	C9	E5
⁸⁷ Rb/ ⁸⁶ Sr ICPMS	0.22	0.21	0.094	0.12	0.080	0.060	0.23	0.053	0.14	0.14	0.14	0.062
⁸⁷ Sr/ ⁸⁶ Sr measured	0.708035	0.711189	0.709547	0.709507	0.709504	0.709911	0.708596	0.708915	0.706846	0.710276	0.706668	0.709599
error: 10–6	6	11	12	23	25	7	12	16	11	13	10	5
⁸⁷ Sr/ ⁸⁶ Sr age corrected	0.707488	0.710653	0.709310	0.709197	0.709097	0.709760	0.708020	0.708781	0.706503	0.709931	0.705862	0.709442
Ages (Ma)	177	177	177	177	177	177	177	177	177	177	177	177

5. Results

5.1. Whole-rock major- and trace-element compositions

5.1.1. Ultramafic samples

All samples are relatively fresh and show low degree of alteration as evidenced by relatively low loss-on-ignition (LOI) values (0.76 to 5.6 wt.%). The major oxides presented here are calculated on a volatile free basis to reduce the effect of element dilution related to serpentinization. The peridotites from Spontang ophiolite complex show low and restricted contents of SiO₂ (41.37–47.66 wt.%) with low abundances of Al₂O₃ (0.54–1.58 wt.%), TiO₂ (0.02–0.07 wt.%), CaO (0.56–2.35 wt.%), moderate Fe₂O₃ (8.7–10.1 wt.%) and high MgO (39.1–45.2 wt.%). The Mg# ([molar ratio of 100 × Mg²⁺/(Mg²⁺ + Fe²⁺)] range from 90.4 to 91.9 and resemble residual oceanic peridotites (Bonatti and Michael, 1989; Bodinier and Godard, 2007). Lherzolites show Mg# ranging between 90.6 and 91.8 with Mg# in harzburgites between 90.4 and 91.9 with the dunites displaying Mg# between 91.0 and 92.0. Al₂O₃ and CaO in the lherzolites vary between 0.68 to 1.36 wt% and 1.19 to 1.81 wt.%, respectively, which is higher than the harzburgites. Dunites contain the lowest Al₂O₃ (0.66–1.36 wt.%) and CaO values (1.15–1.27 wt.%). On the basis of CaO and Al₂O₃ concentrations (Fig. 4a), all samples plot towards the lower end of the abyssal peridotite field with a couple of samples plotting within the fore-arc peridotite field. To understand the degree of depletion, major oxide concentrations were plotted against MgO (Fig. 4b). SiO₂ and CaO display well defined inverse correlations whereas Fe₂O_{3total} and Al₂O₃ show a strong positive correlation. The studied peridotites are enriched in transition elements viz. Cr (1226–12335 ppm), Ni (2076–9001 ppm) Co (102–459 ppm) and Cu (4–76 ppm), much higher than primitive mantle values (Ni > 400 ppm and Cr > 800 ppm), and show a positive correlation when plotted against MgO (e.g. Co). Chondrite-normalized patterns for the studied peridotites reflect low ΣREE concentrations of 0.05 to 0.81 ppm with depleted light rare earth elements (LREE) relative to middle and heavy rare earth elements i.e. (La/Sm)_N = 0.36 to 2.4) and (La/Lu)_N = 0.01 to 0.38) with an exception of the dunite sample (E5). Middle rare earth elements (MREE) are observed to be depleted relative to heavy REE (HREE; (Sm/Yb)_N = 0.03 to 0.99). In the REE diagram (Fig. 4c), the peridotites show gradual decrease from Lu to Sm, however the MREE-HREE concentration in the lherzolites are lower than the harzburgites and dunites. The samples display U-shaped patterns with the lowest points at Nd and then slightly increasing from Pr to Ce and La being relatively flat. The dunites on the contrary, show increasing contents from Eu to La (except sample SP3). In a primitive mantle normalized multi-element plot, the Spontang peridotites display enriched concentrations of moderately to slightly incompatible elements (e.g. Ti and Zr, MREE – HREE). The samples are relatively enriched in large-ion lithophile elements (LILE) viz. Ba, Sr and fluid-mobile elements like U (Fig. 4d).

5.1.2. Mafic samples

Whole-rock geochemical analysis of twelve mafic samples including nine isotropic gabbro samples and three basaltic samples were performed. All samples exhibit low level of alteration (LOI = 0.53–1.01 wt.%) and are characterized by varying concentrations of SiO₂ (49.4–57.1 wt.%) and MgO (4.3–9.5 wt.%). Mg# for the basalts ranging from 63.8 to 70.9 and from 49 to 58 for the gabbroic rocks indicate that they derive from evolved rather than primitive magmas. TiO₂ concentrations vary from 0.66 wt.% to 1.74 wt.% which closely resemble mid-ocean ridge basalt (N-MORB) values (1.61 wt.% on average; Hofmann, 1988). The total alkali (Na₂O + K₂O) contents of the studied samples range between

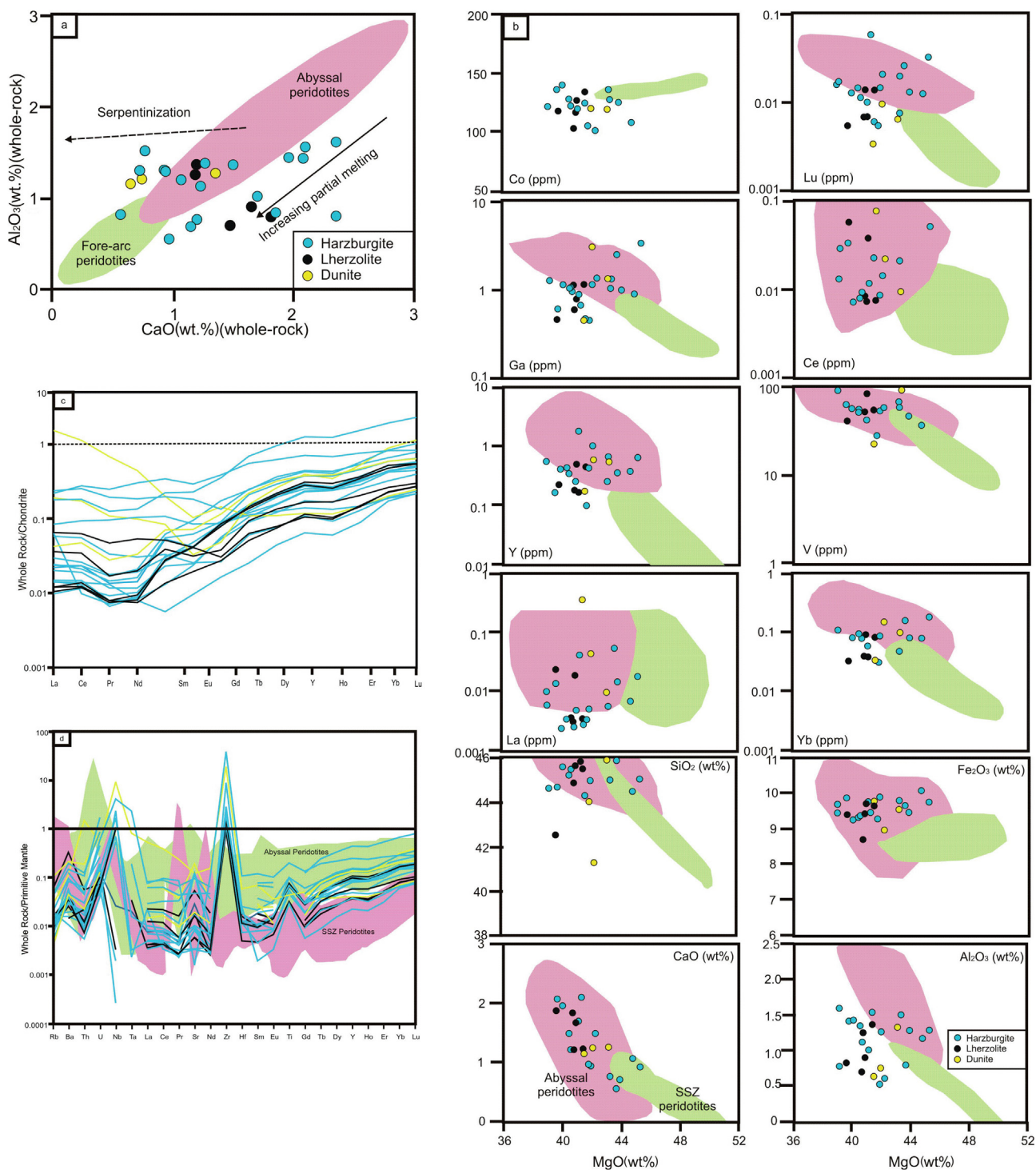


Fig. 4. (a) Whole-rock Al_2O_3 (wt.%) versus CaO (wt.%) plot for the Spontang peridotites. Abyssal and forearc peridotite fields, as well as the partial melting trend, are taken from Pearce et al. (1992). (b) Variation diagrams of major oxides and trace elements vs. MgO (wt.%) in bulk rock Spontang peridotite samples. Abyssal (after Niu et al., 1997) and supra-subduction zone peridotite (after Parkinson and Pearce, 1998) fields are also shown for comparison. (c) Chondrite normalized REE patterns. (d) Primitive mantle normalized multi-element spider diagrams of the peridotites of the Spontang ophiolite complex. Normalizing values are after Sun and McDonough (1989). In Fig. 4d, Abyssal peridotite fields are from Hellebrand et al. (2002), Johnson and Dick (1992) and Niu et al. (1997). SSZ peridotite fields are from Parkinson and Pearce (1998).

3.7 and 6.1 wt.% and are characterized by low K_2O/Na_2O ratios of 0.01–1.8. In the Total Alkali versus Silica diagrams (TAS), the studied basaltic samples plot in the basalt fields whereas the gabbro plot in the gabbro, diorite and syeno-diorite fields (Fig. 5a, b). The gabbros when plotted in the AFM and SiO_2 versus FeO_t diagrams (Fig. 5c, d) plot mainly in the tholeiitic fields with the basalts falling in the calc-alkaline fields. However, all studied mafic sam-

ples plot in the sub-alkaline area when plotted in the Nb/Y versus Ti/Y diagram (Fig. 5e) confirming their mildly alkaline nature.

Major elements like CaO and TiO_2 display positive trends when plotted against $Mg\#$, however SiO_2 and Fe_2O_3 displaying negative trends (See Supplementary Data, Fig. S1). Transition elements like Ni are relatively lower in the studied mafic dykes (79 ppm to 149 ppm) than in primary basalts (Ni = 300–400 ppm; Frey et al.,

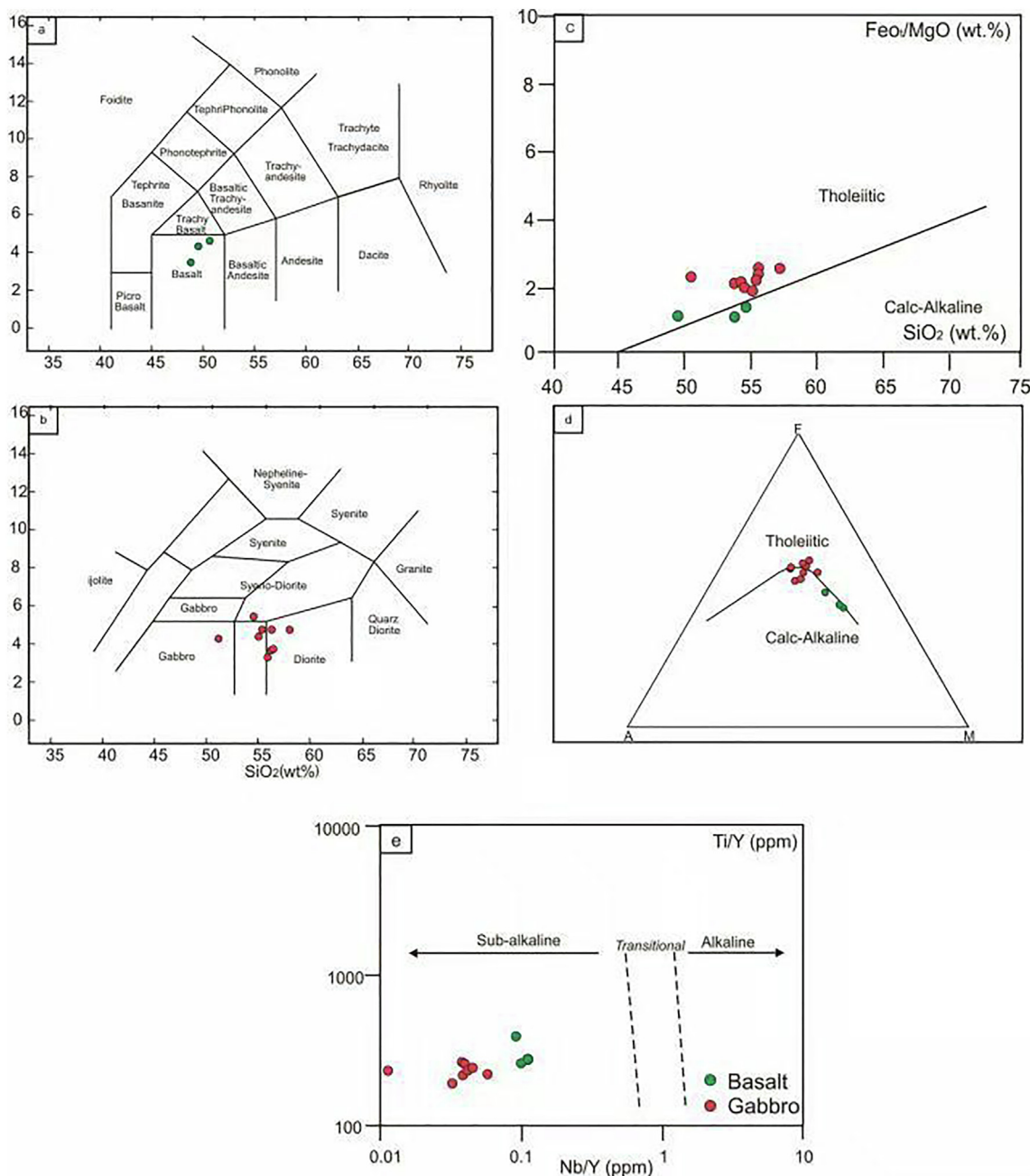


Fig. 5. (a) Classification diagrams of the mafic rocks of the Spontang ophiolite complex. (b) Total alkali versus Silica diagrams (after Le Bas et al., 1986; Cox et al., 1979). (c) SiO₂ (wt.%) versus FeO/MgO. The boundary line between tholeiite and calc-alkaline rock types is from Miyashiro (1974). (d) AFM ternary diagram (Irvine and Baragar, 1971). (e) Nb/Y versus Ti/Y diagram.

1978) whereas Cr contents range between 261 and 347 ppm for the investigated basalts. Mg# when plotted against Zr shows a positive correlation for all samples. Cr and Ni concentrations of the gabbros range from 6 ppm to 58 ppm and 14 ppm to 31 ppm respectively and show a positive trend when plotted against Mg# (See Supplementary Data, Fig. S1) indicating clinopyroxene fractionation. Gabbros have variable total rare earth element (Σ REE) concentrations ranging from 9.46 to 19.3 ppm when compared with the basalts (12.3 to 29.3 ppm). Chondrite-normalized patterns for the studied mafic rocks display smooth flat patterns showing enrichment up to 10 to 30 times that of chondrite values (Σ REE_N = 9 to 29) (Fig. 6a). The gabbros are LREE-depleted ((La/Yb)_N = 0.47 to 0.76 and (La/Sm)_N = 0.52–0.73) with slightly elevated patterns

depicted by the basalts ((La/Yb)_N = 0.71–1.06 and (La/Sm)_N = 0.64–0.79). REE abundances in gabbros are observed to increase from MREE to HREE ((Dy/Yb)_N = 0.97–1.09) similar to normal (N)-MORB like patterns, with the basalt samples showing slightly elevated HREE patterns ((Dy/Yb)_N = 1.09–1.46). All samples exhibit no Eu anomaly (Eu/Eu* = 0.97 on average) indicating absence of plagioclase fractionation. In the N-MORB-normalized incompatible trace-element diagram (Fig. 6b), the gabbro and basalt samples exhibit enriched LILE (Rb, Ba and Sr) typical of subduction related magmas (Pearce and Robinson, 2010). Gabbros exhibit negative Nb-Ta-Ti depletions along with Zr and Hf (not shown) whereas the basalt samples show negative Nb and positive Ta and Ti anomalies.

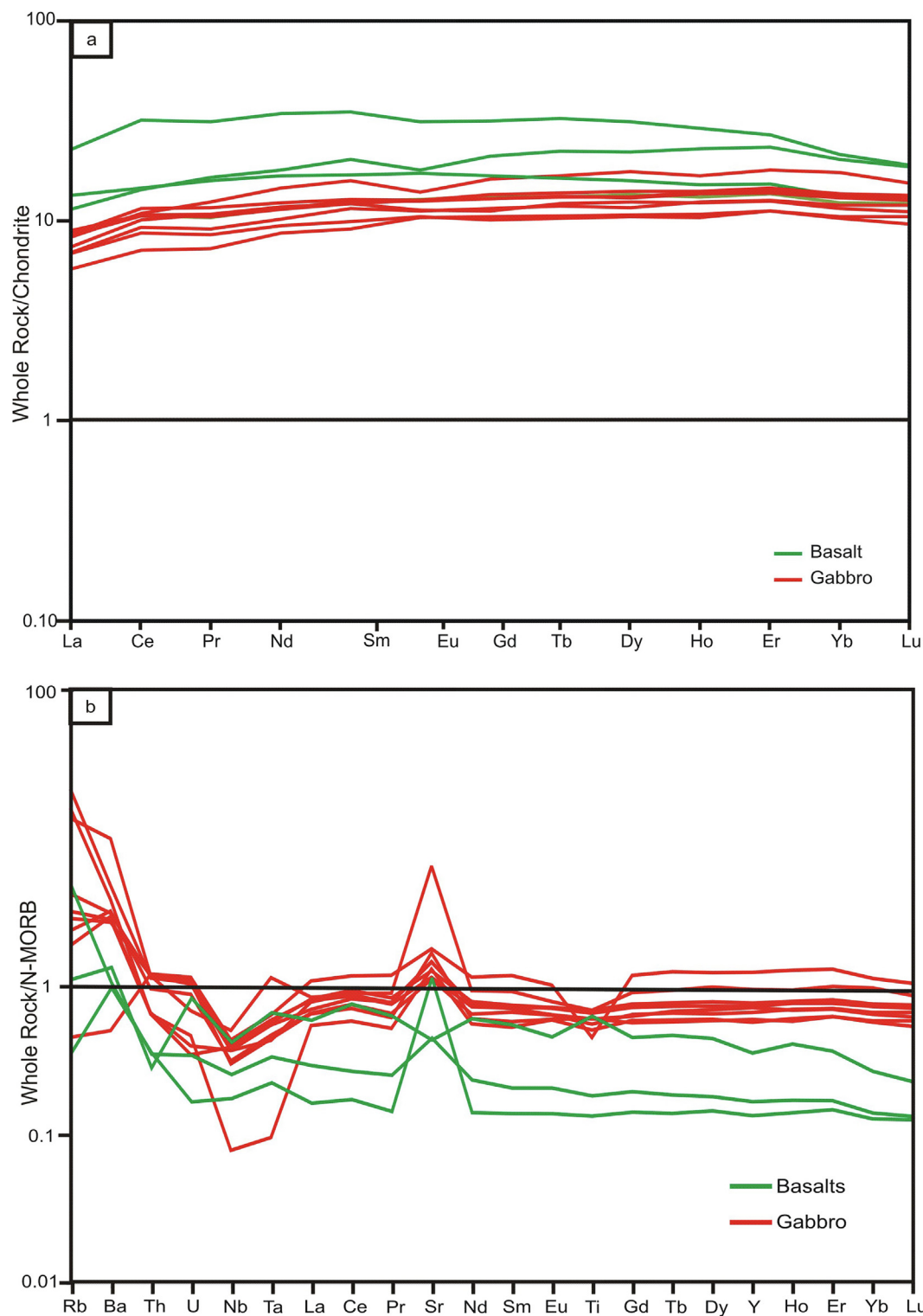


Fig. 6. (a) Chondrite normalized REE patterns. (b) Primitive mantle normalized multi-element spider diagrams of the mafic rocks of the Spontang ophiolite complex. Normalizing values are after Sun and McDonough (1989).

5.2. Whole-rock Sr-Nd isotopic results

A total of twenty-nine samples consisting of fifteen mafic and fourteen ultramafic samples were selected for Sr and Nd isotopic analyses. Three basalts, nine gabbros, one dunite, nine harzburgites and four lherzolites were processed. For the ultramafic series, only Sr isotopes have been determined, the REE content being too low to

allow the extraction of enough Nd for isotopic measurements. The $^{87}\text{Sr}/^{86}\text{Sr}$ and $^{143}\text{Nd}/^{144}\text{Nd}$ have been corrected for radioactive decay using an age $t = 177$ Ma, which is the age proposed by Pedersen et al. (2001) for the Spontang ophiolitic formations. All mafic samples having low $^{87}\text{Rb}/^{86}\text{Sr}$ (typically below 0.2), and similar $^{147}\text{Sm}/^{144}\text{Nd}$, the age corrections have either little or no effect on the corrected isotopic ratios. Except for one sample, (sample

A2, 0.7089), basalts and gabbros display relatively close $^{87}\text{Sr}/^{86}\text{Sr}(t)$ ratios (0.7036 to 0.7048) and radiogenic Nd isotopic compositions ($\epsilon_{\text{Nd}}(t)$) from +6.3 to +8.3, the sample A2 having the least radiogenic value. Ultramafic samples are characterized by elevated initial Sr isotopic ratios (0.7056 to 0.7106), which are partly correlated to $1/(\text{Sr})$ (figure not shown). For those samples, part of their initial Sr isotopic compositions is higher than the $^{87}\text{Sr}/^{86}\text{Sr}$ cretaceous seawater signature. These relatively radiogenic initial $^{87}\text{Sr}/^{86}\text{Sr}$ ratios can be related to an underestimation of the actual time-integrated $^{87}\text{Rb}/^{86}\text{Sr}$ owing to a recent change in their Rb/Sr ratio, as Rb was likely to be preferentially remobilized during greenschist facies metamorphism. Crustal fluid contaminations during the obduction processes may also change the $^{87}\text{Sr}/^{86}\text{Sr}$ ratios of the samples, especially the depleted ones, towards more radiogenic values.

Mafic samples are plotted in the $\epsilon_{\text{Nd}}(t)$ vs $^{87}\text{Sr}/^{86}\text{Sr}(t)$ diagram in order to compare our data to those published, of same petrological affinities, along the Indus Suture Zone (Fig. 7). Both mafic (basalts, andesites and gabbros) and published ultramafic samples define different tendencies as observed in this figure, highlighted by previous authors (Bignold and Treloar, 2003; Bignold et al., 2006; Dhuime et al., 2007; 2009; Zhu et al., 2007; 2008; 2009; Lee et al., 2012; Kang et al., 2014). The positioning of our newly measured samples comparatively to these tendencies will be discussed below. However, it is worth noting that the Spontang samples fall within the most radiogenic reported samples for $\epsilon_{\text{Nd}}(t)$ along the Indus Suture Zone and display typical shift towards radiogenic $^{87}\text{Sr}/^{86}\text{Sr}(t)$ classically attributed to sea water contamination (Lanphere et al., 1981; McCulloch et al., 1981; Benoit et al., 1999). Finally, despite the fact that they display $\epsilon_{\text{Nd}}(t)$ values close to the most radiogenic data obtained by Bignold et al. (2006) and

Dhuime et al. (2007, 2009) for the Kohistan island-arc formations, they also fall within the radiogenic part of Indian MORB domain (Mahoney et al., 1998, 2002), indicating juvenile characteristics of their source.

5.3. Mineral chemistry

5.3.1. Olivine

Olivine from the Spontang peridotites is forsteritic and show limited compositional range from $\text{Fo}_{87.2-91.5}$, avg. $\text{Fo}_{90.3}$ close to those of olivine from abyssal peridotites (average Fo content = 91; Dick and Bullen, 1984). Olivines from both lherzolites and harzburgites show similar Mg# between 90 and 93 while dunites display Mg# contents of 88–92. NiO contents in olivine are variable and range between 0.34 and 0.51 wt.% and 0.25 and 0.49 wt.% in harzburgites and lherzolites, respectively while dunitic olivines display a wider range from 0.04 to 0.53 wt.%. Ca contents in all the studied samples are very low (~0.07 wt.%). MnO contents in lherzolitic olivine range between 0.09 and 0.27 wt.% versus 0.09 to 0.19 wt.% in harzburgites. MnO contents of dunitic olivine vary from 0.01 to 0.22 wt.%. The Fo contents display a positive correlation with NiO (Fig. 8a) and are negatively correlated with MnO (Fig. 8b).

5.3.2. Pyroxenes

Pyroxenes from the studied peridotites are of enstatite and Cr-diopside varieties according to the nomenclature of Morimoto et al. (1988). Enstatite contents range between 84.1 and 90.2 and 85.7 to 89.9 in the harzburgites and lherzolites respectively, while dunitic orthopyroxenes display En contents ranging from 85.6 to 93.7. Similarly, Mg# of orthopyroxene in harzburgites (88.1 to

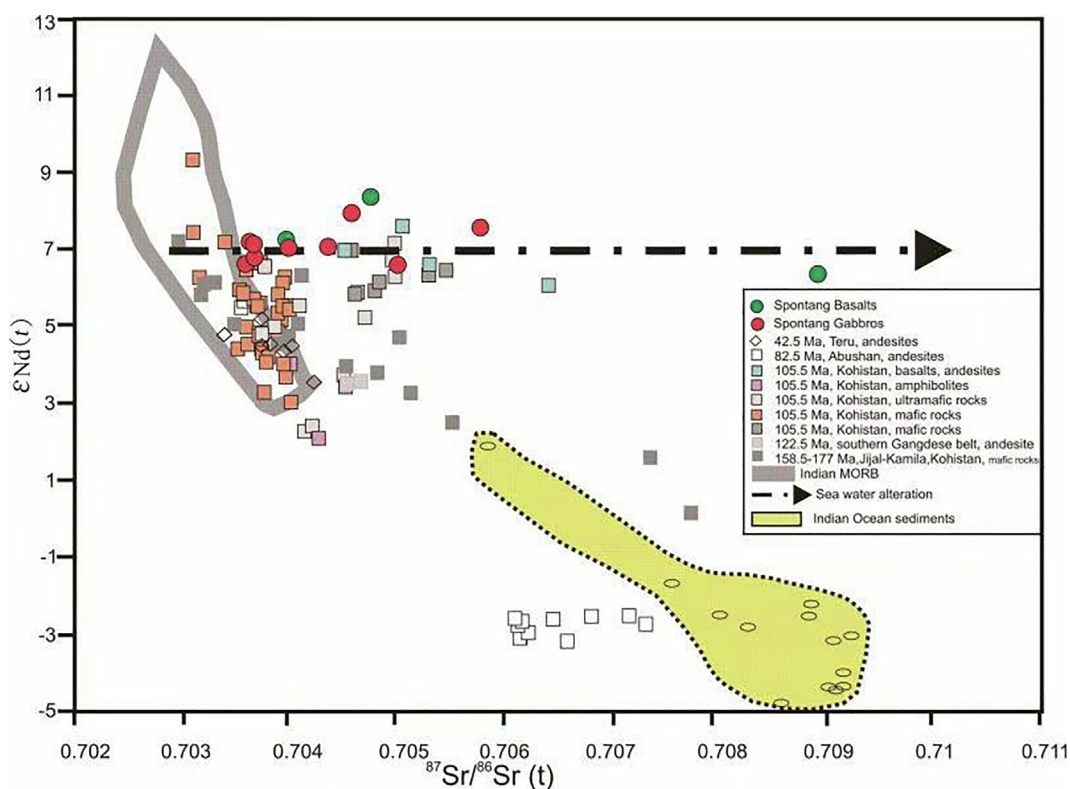


Fig. 7. $\epsilon_{\text{Nd}}(t)$ vs $^{87}\text{Sr}/^{86}\text{Sr}(t)$ diagram for Spontang basalts and gabbros, superimposed on available isotopic data for mafic and ultramafic rocks from the ITSZ (Khan et al., 1997; 2004; Bignold and Treloar, 2003; Bignold et al., 2006; Dhuime et al., 2007, 2009; Zhu et al., 2009; Kang et al., 2014; Li et al., 2015). All isotopic data have been age-corrected according their measured or estimated emplacement ages (177 Ma, Pedersen et al., 2001 for Spontang samples). Actual, Indian MORB domain and actual sediments, extracted from Earthchem database (<http://www.earthchem.org/>) are also reported. The dotted lines illustrated the Cretaceous Sea water contamination trend (triple bold), the Oceanic Arc (bold dotted) and Continental (double dotted) mixing trends.

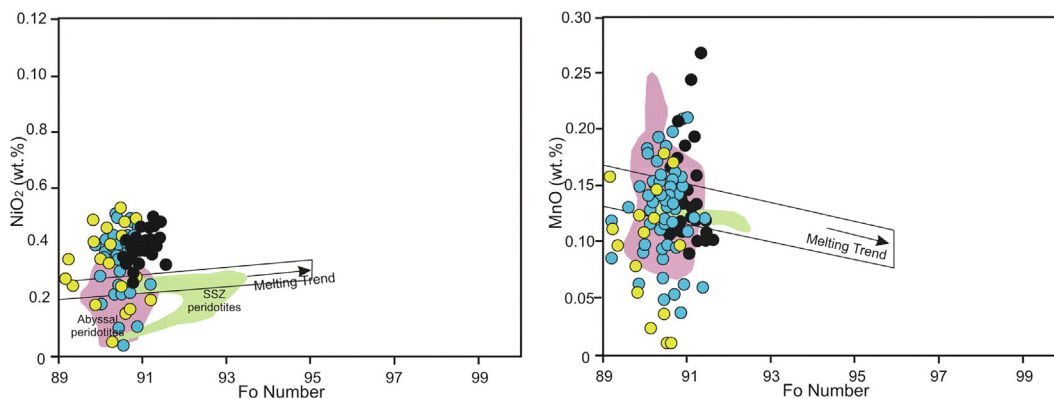


Fig. 8. Compositional variation plots of olivine (Fo content) versus NiO(a), and MnO(b). Partial melting trends are from Ozawa (1994), abyssal peridotite and fore arc peridotite are from Pagé et al. (2008).

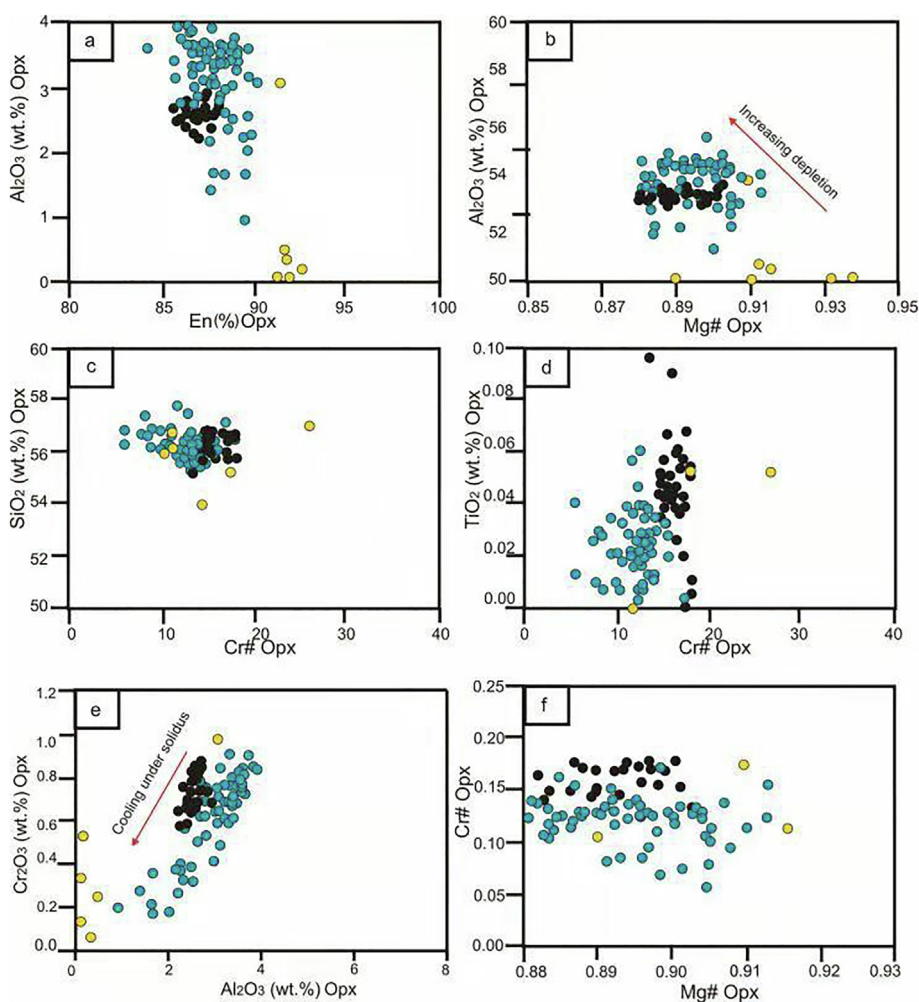


Fig. 9. Compositional variation plots of orthopyroxene (a) En% versus Al₂O₃ (wt.%); (b) Mg# versus Al₂O₃ (wt.%), Cr# versus; (c) SiO₂ (wt.%) and (d) TiO₂ (wt.%). (e) Al₂O₃ (wt.%) versus Cr₂O₃ (wt.%). (f) Mg# versus Cr#.

91.3) is relatively higher than that in lherzolites (88.1–90.5). Orthopyroxene Al₂O₃ contents are variable and range between 1.63 and 3.89 wt% in the harzburgites, with relatively close values in the lherzolites (2.21–2.93 wt%) and are negatively correlated with En and Mg# content (Fig. 9a, b). Orthopyroxenes from lherzolites display similar Cr₂O₃ and MnO contents (0.37–0.87 wt.%; 0.09–0.19 wt.%) comparable to the harzburgites (0.22–0.91 wt.%;

0.08–0.20 wt.%) and exhibit higher CaO contents (0.32–0.68 wt.%) when compared with the harzburgites (0.26–1.30 wt.%).

Cr# (Cr# = Cr/(Cr + Al)) are high in lherzolites (0.13–0.18) compared to the harzburgites (0.74–0.17) and are negatively correlated with SiO₂ (Fig. 9c) and Mg# (Fig. 9f). TiO₂ ranges between 0.03 and 0.11 wt% in both peridotites varieties and show a positive correlation when plotted against Cr# (Fig. 9d). In both peridotite types,

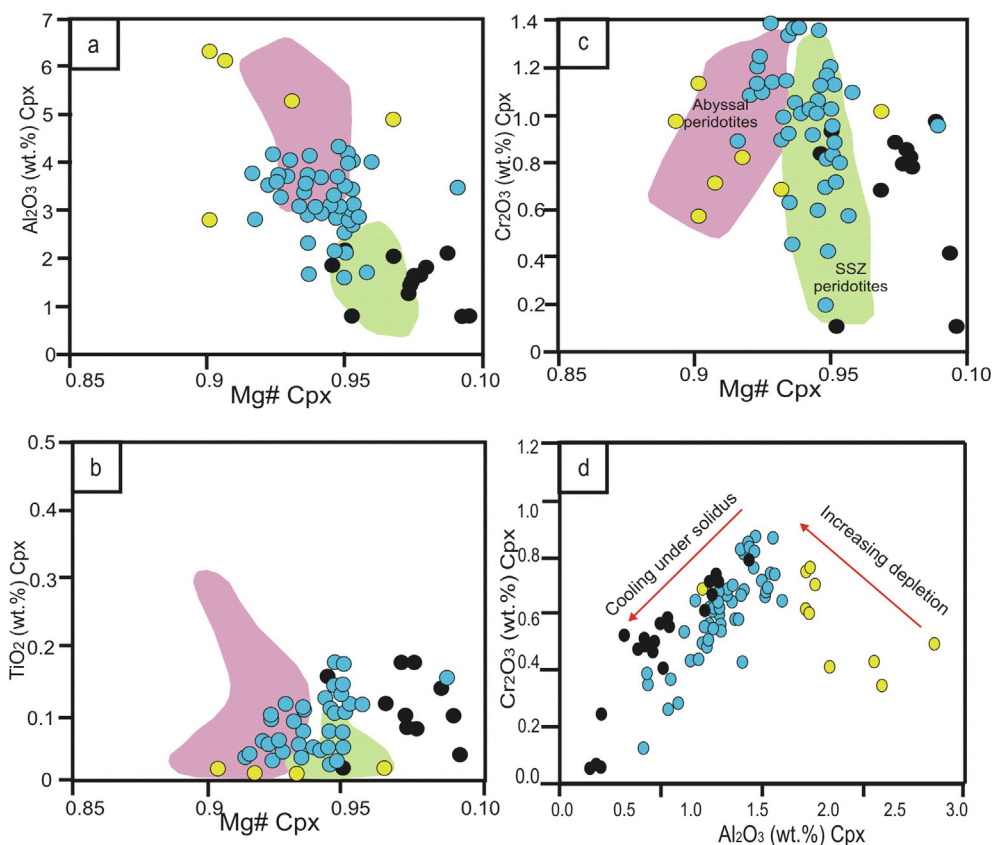


Fig. 10. Compositional variation plots of clinopyroxene (a) Mg# versus Al₂O₃ (wt.%), (b) TiO₂ (wt.%), (c) Cr₂O₃ (wt.%), (d) Al₂O₃ (wt.%) versus Cr₂O₃ (wt.%). Abyssal peridotites are after Johnson et al. (1990) and forearc peridotites are after Ishii et al. (1992).

the opx grains have lower Al₂O₃ (Fig. 11a) and Cr₂O₃ (Fig. 10d) contents and high Mg# values (Fig. 9e, f) possibly as a result of re-equilibration during subsolidus cooling (Xiong et al., 2017).

Clinopyroxenes from the studied peridotites are chemically homogeneous diopsides with average compositions of En₄₅₋₇₄Wo₂₇₋₅₁Fs₆₋₁₅. Clinopyroxenes from lherzolites display high Al₂O₃ (1.68–4.40 wt.%) and Cr₂O₃ contents (0.41–1.30 wt.%) comparable to those of harzburgites (Al₂O₃ = 1.64–4.25 wt.%; Cr₂O₃ = 0.20–1.44 wt.%). The Mg# values of clinopyroxenes in harzburgites show a more varied range from 88.7 to 96.5 in comparison to the Mg# displayed by clinopyroxenes from the lherzolite samples (89.8–95.1). In both peridotite types, the cpx grains have lower Al₂O₃ (Fig. 10a) and Cr₂O₃ (Fig. 10d) contents and high Mg# values (Fig. 10a–c) possibly as a result of re-equilibration during subsolidus cooling (Xiong et al., 2017). Cr# in Cpx from harzburgites (0.78–0.21) are lower than those of the lherzolitic Cpx (0.74–0.31). TiO₂ content of clinopyroxenes is positively correlated with Mg# and is higher in the lherzolites (0.09 wt.% to 0.21 wt.%) than in the harzburgites (0.03 wt.% to 0.18 wt.%) (Fig. 10c). Similarly, Na₂O content of clinopyroxene in lherzolites is higher (0.08–0.53 wt.%) than those in harzburgites (0.002–0.30 wt.%). Dunitic clinopyroxenes show negligible TiO₂ contents and low Na₂O contents.

5.3.3. Spinel

Detailed presentation of chemical compositions of spinels from the studied peridotites is available in Jonnalagadda et al. (2019) and is summarized below. Spinel is classified as spinel – spinel-hercynite and display high Cr₂O₃ and low TiO₂ contents confirming their depleted character. Al₂O₃ contents vary between

37.60–43.9 wt.% in the spinel from dunites while those from the lherzolites and harzburgites display Al₂O₃ values ranging from 23.8 to 35.6 wt.% and from 33.2 to 62.4 wt.%, respectively. Cr# in the spinel's from lherzolites are moderately low (0.10–0.34) especially in comparison to Cr# from dunitic spinels (Cr# = 0.79). Mg# decreases with increasing Cr# (Fig. 11a). Based on the Cr# versus Fo content of spinel – olivine pairs, all peridotite samples plot within the mantle array (Arai, 1994a, b) (Fig. 11b). Low TiO₂ contents observed in the spinels of the studied peridotites (0.1–0.3 wt.%) are consistent with their residual nature.

5.4. Mineral trace-element compositions

5.4.1. Olivine

Studied olivines are characterized by low Ca (177 to 362 ppm) and Ti contents (3.82 to 9.26 ppm) and fall within the established range of mantle derived olivines (Ca > 700 ppm, Ti > 70 ppm; Foley et al., 2013). Trace-element compositions of olivine from the studied peridotites display very low concentrations close to the detection limits and hence the observations are not relevant and not discussed further.

5.4.2. Clinopyroxenes

Trace-element including REE compositions of clinopyroxenes from the Spontang lherzolites and harzburgites differ from those of cpx from depleted MORB-source mantle (DMM). In the chondrite-normalized REE diagram (Fig. 12a), clinopyroxenes from the harzburgites and lherzolites display smooth patterns with depleted LREE and a gradual increase in MREE with enriched HREE above chondritic values. In the primitive-mantle-normalized dia-

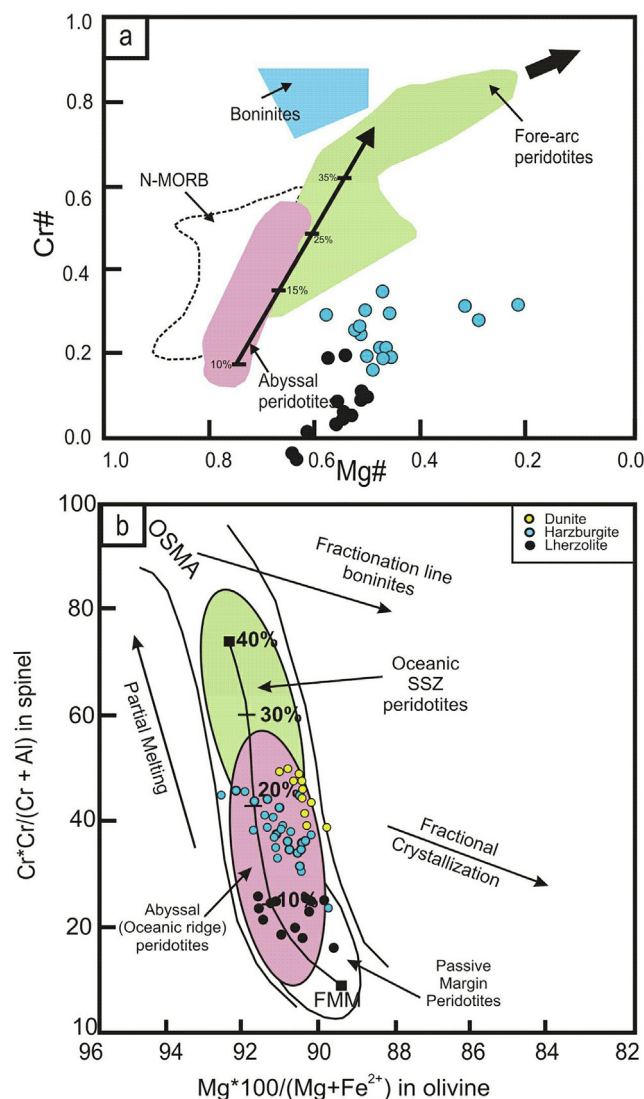


Fig. 11. Spinel compositions of the Spontang peridotite samples plotted on (a) Mg# [100 × Mg/(Mg + Fe²⁺)] vs. Cr# [100 × Cr/(Cr + Al)] diagram. Data for spinel in modern abyssal peridotites is from Dick and Bullen (1984) and Juteau et al. (1990). Field for spinel in boninites is taken from Dick and Bullen, (1984). Data for spinel in fore-arc peridotites are from Ishii et al. (1992) and Ohara and Ishii (1998). Partial melting trend (black arrow) is from Arai (1994). (b) Cr# in spinel versus Fo content of olivine in peridotites of Spontang ophiolite. Fields for spinels occurring in abyssal (and ocean ridge), oceanic SSZ and passive margin peridotites are after Dick and Bullen (1984) and Pearce et al. (2000). OSMA means Olivine Spinel Mantle Array and fractionation line of boninites are after Arai (1994a, b).

gram (Fig. 12b), clinopyroxenes show overall depleted patterns with negative Ba, Th, Sr and Zr anomalies and slightly positive anomalies in U, Ta, Nb, Hf and Ti.

5.4.3. Orthopyroxenes

Orthopyroxenes of the Spontang peridotites are more depleted than the DMM. HFSE of orthopyroxenes from both peridotite varieties pronounced depletion in Zr, Nb, Ta and positive enrichments in Ti and Hf. In the chondrite-normalized REE patterns (Fig. 12c), orthopyroxenes from the lherzolites and harzburgites are characterized by depleted LREE and a gradual increase from MREE to HREE. In the primitive-mantle-normalized diagram (Fig. 12d), all samples show obvious negative anomalies of Ba, La, Sr, Zr while U, Hf and Ti, show positive anomalies.

5.5. Temperature estimates

Equilibration temperatures for the Spontang peridotites have been calculated using co-existing mantle phase compositions. The Spontang peridotites are plagioclase- and garnet-free spinel-facies peridotites for which no robust geobarometers exist. The following thermometers have thus been used assuming a pressure of 1.5 GPa typical of upper mantle peridotites within the spinel stability field (Gasparik, 1987). (1) Fe-Mg exchange between Opx and Cpx (T_{BK90} ; Brey and Köhler, 1990); (2) Ca in Opx (T_{BKCa90} ; Brey and Köhler, 1990) and (3) Fe-Mg exchange between olivine and spinel (Fabries, 1979). Using the thermometers based on the Ca and Fe-Mg exchange in pyroxenes, average temperature estimates for the lherzolites are $T_{BKCa90} = 779\text{--}1046\text{ }^{\circ}\text{C}$ and $T_{BK90} = 762\text{--}1054\text{ }^{\circ}\text{C}$ respectively. In contrast, the harzburgites record lower temperatures ($T_{BKCa90} = 519\text{--}996\text{ }^{\circ}\text{C}$ and $T_{BK90} = 730\text{--}1006\text{ }^{\circ}\text{C}$). Using the partitioning of Mg and Fe²⁺ between olivine and spinel, the calculated temperatures range from 646 °C to 795 °C, significantly lower than the pyroxene-based thermometers. The Spontang lherzolites thus have systematically higher equilibration temperatures than coexisting harzburgites using pyroxene-based thermometers while thermometers using olivine and spinel give similar temperatures for both peridotite varieties. For the samples for which both cpx and opx trace-element compositions were available (two harzburgites and one lherzolite), the REE in two-pyroxene thermometer of Liang et al. (2013) was also applied. The temperature inversions were restricted to the HREE and Y while the LREE visibly deviate from a linear regression, most likely affected by secondary processes and/or poor analytical precision due to their low abundances in opx. The harzburgites yield $T_{REE} = 1115$ and $1277\text{ }^{\circ}\text{C}$, but only the former value corresponds to a robust regression passing through the origin (see Supplementary Data, Fig. S2), while the latter may indicate some extent of disequilibrium between cpx and opx. In comparison, the lherzolite yields $T_{REE} = 1216\text{ }^{\circ}\text{C}$, which is significantly higher than the reliable value obtained for the harzburgites. These relatively high temperatures potentially indicate that harzburgites and lherzolites were only little affected by sub-solidus re-equilibration. Limited cooling is also indicated by the overall agreement, at least for the lherzolites, between T_{REE} (1216 °C) and T_{BKCa} (779–1046 °C), considering that REE closure temperatures are commonly higher than major-element ones (e.g. Le Roux et al., 2016; Tilhac et al., 2016). However, this interpretation is not entirely consistent with the differences observed between T_{BKCa} and T_{BK} , although these may simply reflect pressure and compositional dependencies, such as the influence of Na on the Ca content in opx (Nimis and Grütter, 2010).

6. Discussion

6.1. Effects of alteration

Based on petrographic and geochemical studies carried out, evidences of alteration in the studied Spontang samples cannot be ruled out leading us to assess their potential effect on the mobility of key elements. It is known that LILE concentrations such as Sr and Rb could be affected by seawater alteration and low-grade metamorphism of ocean floor rocks. In contrast, immobile elements such as high field strength elements (HFSE; Nb, Ta, Zr and Hf) and REE which commonly are less affected by low-grade hydrothermal alteration and metamorphism (Thompson, 1973; Sheraton, 1984; McCulloch and Gamble, 1991; Pearce et al., 2000) provide good insights on primary igneous processes (Pearce and Norry, 1979). In the Fig. 13, the studied mantle peridotites plot below the mantle array implying a possible loss of Mg during hydrothermal metamorphism (Niu, 2004). To test this

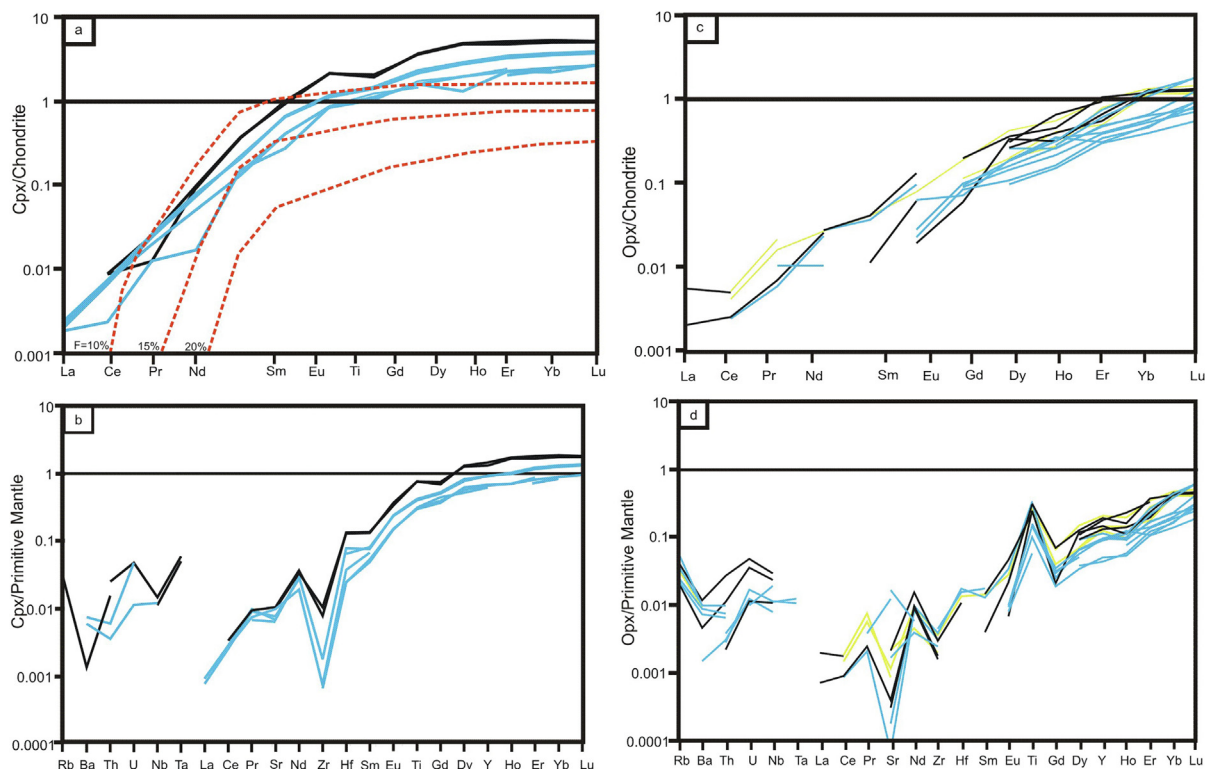


Fig. 12. (a) and (c) REE and (b) and (d) multi-element patterns of clinopyroxenes and orthopyroxenes in representative Spontang peridotites, normalized to values for chondrites and the primitive mantle Sun and McDonough (1989), respectively. Red dashed curves in Fig. 12a represent the modelled REE compositions of residual clinopyroxenes [melting degrees (F) of 10%, 15%, and 20%] after perfect nonmodal fractional melting within spinel-facies mantle, described by Hellebrand et al. (2002).

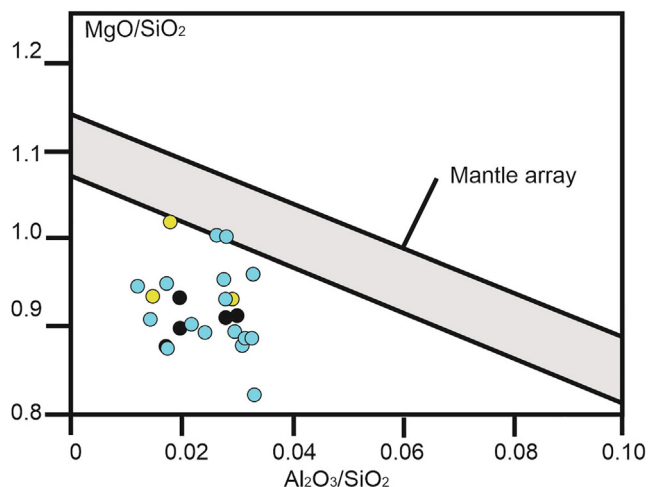


Fig. 13. Mantle array plot of MgO/SiO₂ versus Al₂O₃/SiO₂ diagram of Spontang peridotites. Mantle array is from Hart and Zindler (1986).

further, Al₂O₃ is used as a depletion index to constrain the behavior of major elements (Snow and Dick, 1995). Major oxides like SiO₂ (Fig. 14) along with transition elements like Cr and Ni display a positive correlation when plotted against Al₂O₃ whereas the negative trend observed between Al₂O₃ and MgO is typical of residual mantle rocks (Niu, 2004). Binary plots of immobile HFSE and their neighboring REE, e.g. Hf against La, Ce and Yb in the studied peridotites indicate that LREE were immobile during alteration and primarily controlled by magmatic processes (Niu, 2004; Paulick et al., 2006) (Fig. 15). In the mafic rocks, behavior of Zr (Fig. 16) against major oxides like TiO₂, Fe₂O₃, P₂O₅ and REE like Y and Ce (not

shown) display good positive trends implying that these elements were immobile during alteration. Transition elements like Ni and V also display a positive correlation when plotted against Zr.

Sea water contamination is known to have an effect on Sr isotopic compositions in ophiolites, which is classically characterized by a horizontal drift in Sr-Nd space towards more radiogenic values (Lanphere et al., 1981; Benoit et al., 1999). Upper Cretaceous seawater has an isotopic Sr composition of about 0.709 (Spooner, 1976, Burke et al., 1982) and therefore, during seafloor high temperature (HT) water circulations or late HT/LP metamorphism, samples may lose their pristine magmatic isotopic signatures, according to the water/rock ratios and initial Sr concentrations. However, this low-grade metamorphism has no or little effect on the Nd isotopic ratios (Benoit et al., 1999; Nonnotte et al., 2005), which therefore can be used to discuss high-temperature mantle processes. It is worth noting that for both mafic and ultramafic series, the drift in Sr isotopic signatures is inversely proportional to their Sr concentrations, confirming that seawater contamination can be approximated by simple mixing processes. As a consequence, the ultramafic rocks (i.e. with the lowest primary Sr concentrations) are highly affected, despite their paleo-depth in the ophiolitic section.

6.2. Partial melting

Mineral chemistry along with whole-rock geochemical compositions of upper-mantle peridotites can be instrumental to decipher the extent of partial melting as well as melt/fluid phase enrichment and mantle-melt interaction processes subsequent to melt extraction (e.g. Johnson et al., 1990; Hellebrand et al., 2002; Seyler et al., 2007; Uysal et al., 2007; 2012; Choi et al., 2008; Dilek and Morishita 2009; Morishita et al., 2011). Based on the mineral major-element compositions, it is evident that the

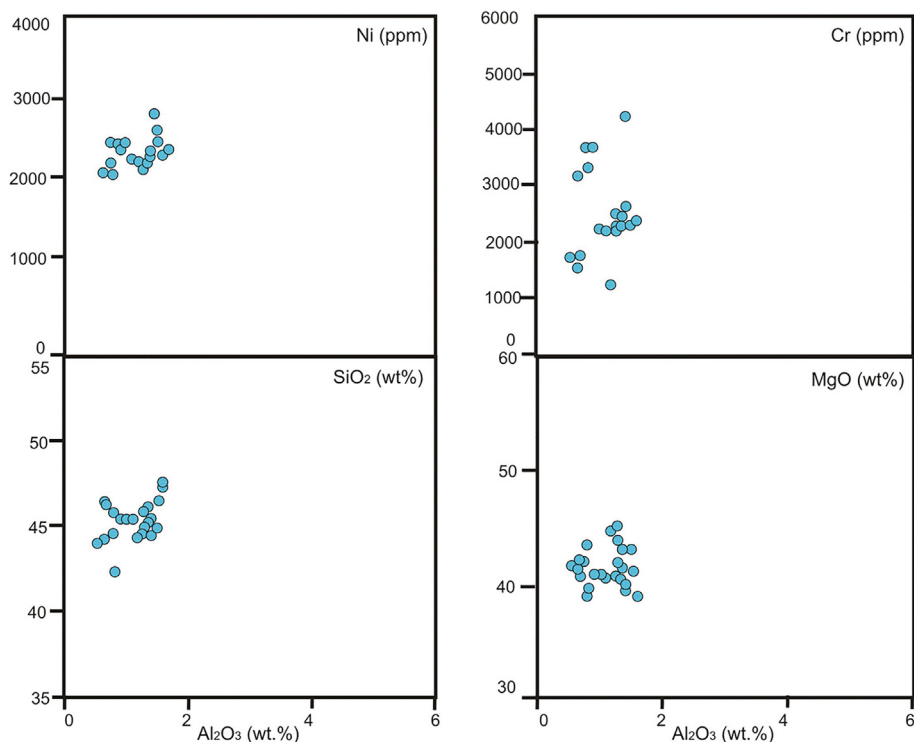


Fig. 14. Variation diagrams of major oxides, trace elements and REE versus Al_2O_3 (wt.%) of Spontang peridotites.

Spontang peridotites were subjected to differing degrees of partial melting (Jonnalagadda et al., 2019). Cr# contents in spinel as well as Al contents in clinopyroxene reflect the relative degree of partial melting (e.g., Hellebrand et al., 2001) and are observed to decrease with the degree of depletion (e.g. Dick and Natland, 1996; Zhou et al., 2005). Using the Hellebrand et al., (2001) equation ($F = 10 \times \ln(\text{Cr}\#) + 24$), fractional melting of the studied peridotites was estimated at around 12–14% for the lherzolites and 17–21% for the harzburgites and about 23% for the dunites. These estimates of partial melting degree are similar to those obtained by using the Mg# versus Cr# plot and the Olivine-spinel mantle array plot (OSMA: Arai, 1994a, b). Al_2O_3 contents of clinopyroxene within the Spontang peridotites show negative correlation when plotted against Cr# of spinel (Fig. 17a) whereas in the Al_2O_3 versus TiO_2 plot, the studied samples show variations consistent with an increase of the degree of partial melting (Fig. 17b). Al_2O_3 , Cr_2O_3 and TiO_2 contents of pyroxenes from the lherzolites are lower than those of the harzburgites with higher Mg# and Cr# values (Fig. 10). In addition, weakly to moderately incompatible elements (e.g. MREE-HREE, Y, Hf, Ti) concentrations in both pyroxenes show that the harzburgites are depleted when compared to the lherzolites suggesting primary control by partial melting process. The lherzolites resemble abyssal type peridotites which underwent depletion in a mid-ocean ridge system while the harzburgites and dunites are analogous to supra-subduction zone (SSZ) peridotites owing to the relatively high degrees of melting recorded by their whole-rock and mineral chemistry.

Trace-element contents in whole rock as well as in pyroxenes were used to perform several melting and enrichment models. We compare the studied lherzolites to closed system dynamic melting model of a PM source (after Palme and O'Neill, 2004). In the Ni/Yb versus Yb diagram (Fig. 18a), the lherzolites are residual of up to 6–8 percent partial melting of the PM whereas the harzburgites range from 8 up to 15 % partial melting. When an open-system dynamic melting models was applied using Model B (from Eiler et al., 2000, 2007), the clinopyroxenes from the

harzburgites show higher degrees of partial melting while when modelled on La/Yb versus Yb diagram (Fig. 18b) and point out around 15 to 17% partial melting. This is in-fact consistent with fractional melting results using whole rock as well as major oxide mineral chemistry. The clinopyroxenes from the lherzolites have in fact negligible La contents and hence were not shown in the above figure (Fig. 18b).

6.3. Melt-peridotite interaction and metasomatic signature

Mantle peridotites containing spinels with $\text{Cr}\# > 0.70$ are believed to result from high degrees of partial melting resulting in pyroxene-free dunites (Kostopoulos, 1991). The Spontang dunites however, contain spinels with high Cr# of 0.79 and low TiO_2 contents (0.05–0.1 wt.%) along with minor interstitial clinopyroxenes that may result from fertilization processes as proposed by Barth et al. (2003) and Godard et al. (2008). Relationship between spinel Cr# and trace-element compositions in the studied pyroxenes were investigated in order to understand if the peridotites were affected by metasomatic and/or partial melting processes. Incompatible trace elements like Yb, Ti, Hf and Zr contents in the clinopyroxenes from lherzolites and harzburgites display a positive correlation when plotted versus spinel Cr# indicating that the host rocks may have been affected by late-stage fluid/melt metasomatism, as un-metasomatized abyssal peridotites would ideally display gradually decreasing trends in the same plots (Bodinier and Godard, 2004; Warren, 2016) (Fig. 19). The Spontang peridotites exhibit REE patterns which are U-shaped, depleted in MREE and variably enriched in LREE, especially the harzburgites and dunites, which display enriched LREE and other highly incompatible elements (like Ba, Sr, Zr, Nb, Ti, Th, and U, the latter being a fluid-mobile element) when compared with the lherzolites. Such elevated concentrations of LREE and other incompatible elements clearly reflect that the harzburgites were affected by metasomatic enrichment; an observation a priori not consistent with their higher depleted nature, but in agreement with enrichment due to

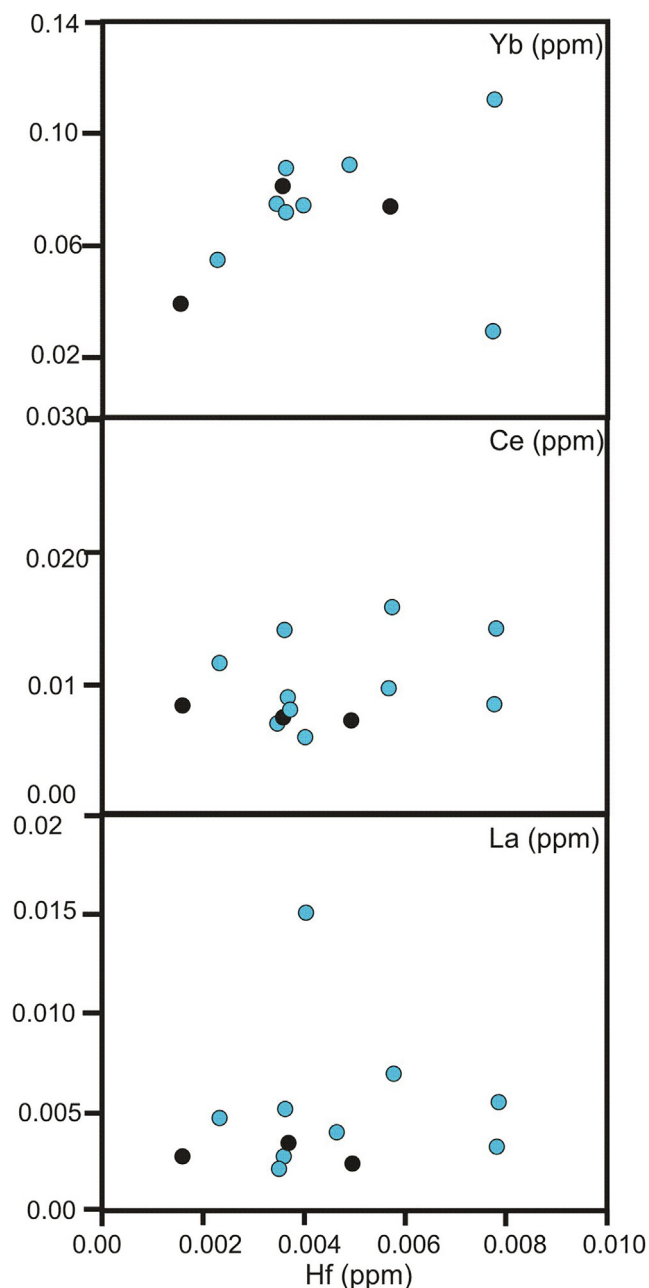


Fig 15. Variation diagrams of Hf versus La (ppm), Ce (ppm) and Yb (ppm) of Spontang peridotites.

late metasomatic events. REE and other trace element compositions of both pyroxenes from the harzburgites show similar enrichments in incompatible and fluid mobile elements like Rb, Th, U, LREEs (except La), Nd, Hf, Ti with MREE-HREE's. In summary, both whole-rock trace-element and REE patterns from the Spontang peridotites indicate that the enrichment in incompatible trace elements as well as LREE reflect at least two processes i.e. mantle-melt interaction that may have resulted in U-shaped REE patterns as well as enrichment in LREE following initial partial melting (depicted by MREE- HREE patterns) by low-degree partial melts derived from a deeper mantle region and reacting with the overlying depleted mantle. Positive spikes in U, detectable Ba, depleted Zr and negligible Nb and Ta signatures observed in the pyroxenes indicate that the studied samples have been metasomatized.

6.4. Nature of the magma sources

Considering their immobile nature during subduction, HFSE's such as Nb, Zr, Ta and Ti are useful to decipher the nature of the magma source (Pearce and Cann, 1973; Pearce and Peate, 1995; Xu et al., 2003; Pearce, 2005; Pearce and Stern, 2006). Geochemical signatures such as enriched LILE and depleted HFSE observed in the Spontang mafic rocks indicate that they could be derived from subduction related magmas. The studied samples exhibit minor REE fractionation with La/Yb_N ratios ranging between 0.47 and 1.06 and low $(Dy/Yb)_N$ (0.97–1.46), $(Sm/Yb)_N$ (0.88–1.63) and $(La/Sm)_N$ (0.52–0.79) ratios. In the Zr versus Nb plot, the samples are observed to plot in the depleted mantle field, indicating derivation from a depleted mantle source (Fig. 20a). When plotted in the La/Yb versus Dy/Yb diagram, the samples fall near the N-MORB domain within the spinel lherzolite fields (Fig. 20b) indicating derivation from a spinel-peridotite mantle source. This trend is consistent in the Nb/Yb versus Th/Yb, TiO_2/Yb and Zr/Yb diagrams (See Supplementary Data, Fig. S3) along with negative Na, Ta and positive LILE anomalies in gabbros indicating that some subducted material contaminated their mantle source (Pearce, 2008). The $(Ta/La)_{PM} = (0.16–1.20)$ and $(Hf/Sm)_{PM} = (0.56–0.87)$ ratios of the studied mafic rocks link them to the depleted upper mantle but indicate that the mantle source was metasomatized by subduction-related fluids (Fig. 21a). However, as shown in the Th/Zr versus Hf/Sm plot (Fig. 21b), the samples follow the melt addition trend as a result of low Th/Zr and high Hf/Sm values implying that the mantle source was enriched following metasomatic processes (Kepezhinskis et al., 1997). The Spontang mafic rocks display Sr/Nd ratios (19.06–85.16) higher than that of N-MORB (12.33; Sun and McDonough, 1989) as well as the upper crust (11.85; Xu, 2014) implying an origin from magmas originated from a source modified by slab-derived fluids. Therefore, contamination of a mantle source by addition of subducted oceanic sediment-derived melts cannot be ruled out as it can increase concentrations of relatively immobile elements like Th and LREE (Woodhead et al., 2001; Xu, 2014). Th/Yb ratios observed in the mafic samples are relatively higher than N-MORB values (0.04; Sun and McDonough, 1989) implying that the magma source was modified by sediment-derived melts.

6.5. Isotopic constraints

Spontang mafic samples are characterized by systematically elevated $\epsilon_{Nd}(t)$ and variable $^{87}Sr/^{86}Sr(t)$. Compared to the available data on mafic lithologies of the Indus Suture Zone (Khan et al., 1997; 2004; Bignold and Treloar, 2003; Bignold et al., 2006; Dhuime et al., 2007, 2009; Zhu et al., 2007; 2008; Li et al., 2015), the studied samples plot along a single seawater contamination line, and do not present any clear isotopic evidence of oceanic sediments participating in their genesis (Fig. 8). It is worth noting that part of Kohistan mafic and ultramafic samples analysed by Dhuime et al. (2007, 2009) display radiogenic Nd isotopic compositions close to those from this study, typically referred to as Type-1 by these authors. In their scenario, Type-1 magmatic event corresponds to the initiation of an intra-oceanic subduction system. Therefore, a depleted mantle source slightly contaminated by sediment-related fluids cannot be ruled out for Spontang mafic samples. However, no isotopic evidence of source evolution through time, like proposed by Dhuime et al. (2009) or Bignold et al. (2006) for the Kohistan magmas, is found in the Spontang mafic samples. All analyzed basalt and gabbro samples in this present study have radiogenic Nd isotopic compositions. In that sense, the source of Spontang melts may be simply MORB-related. In order to test the hypothesis of an upper mantle which may have been contaminated by a plume, as it has been proposed for the

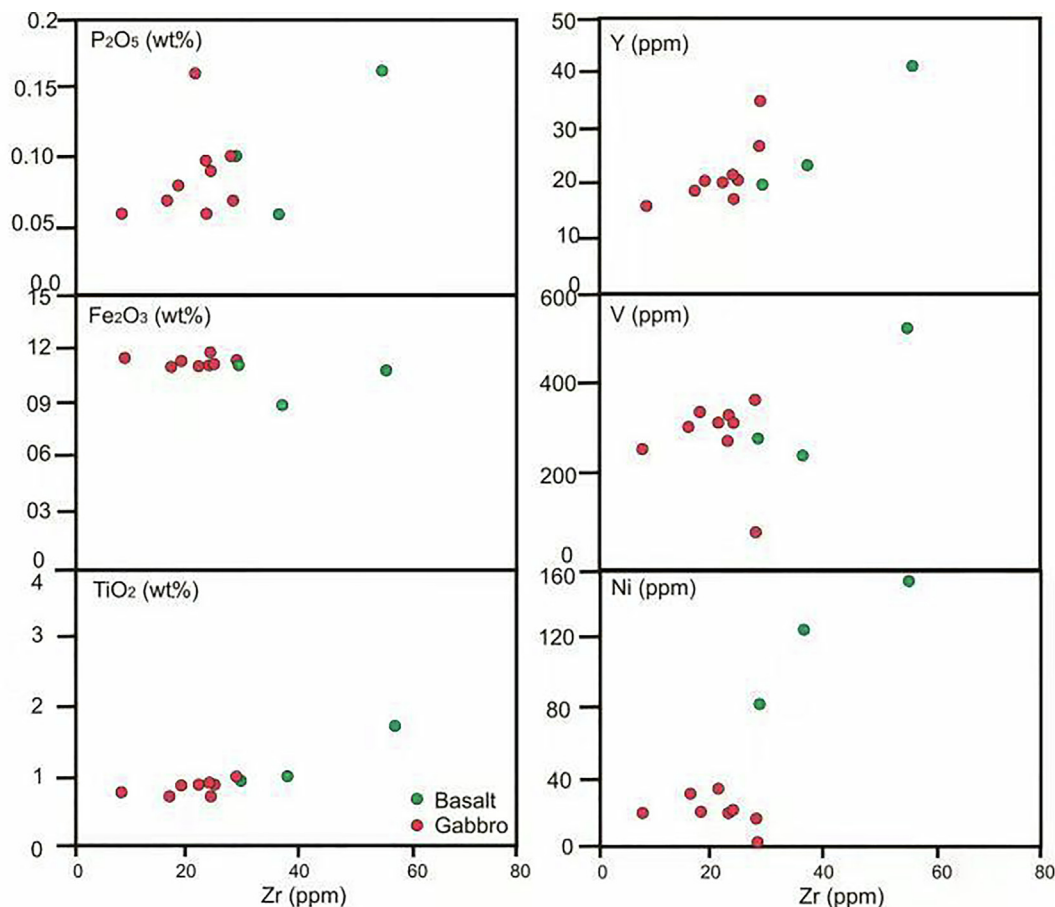


Fig. 16. Variation diagrams of Zr (ppm) versus major oxides and trace elements of mafic rocks of Spontang ophiolite complex.

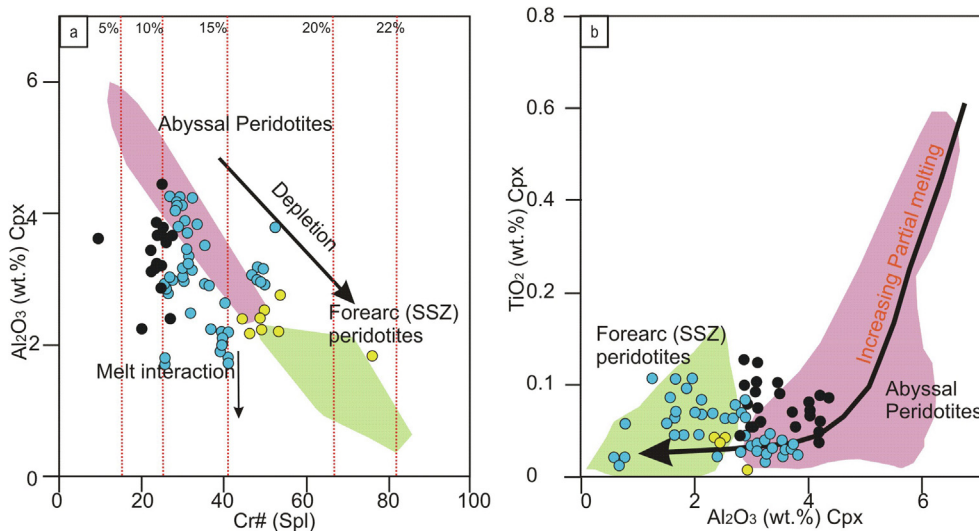


Fig. 17. Variation diagrams of a) Al_2O_3 (wt.%) clinopyroxene versus $Cr\# [100Cr/(Cr + Al)]$ of coexisting spinel. b) TiO_2 (wt.%) versus Al_2O_3 wt.% contents in clinopyroxene of the Spontang peridotites.

Cona massif by Zhu et al. (2008) for Late Jurassic or early Cretaceous mafic magmatism, we have reported our data in the $\epsilon_{Nd}(t)$ vs $(Nb/La)_{PM}$ plot (Fig. 22). In this diagram, the Spontang gabbros and basalts fall on the right-hand side of the MORB towards the arc trend and do not show any evidence of an upper mantle, plume-contaminated, source. Furthermore, they are characterized

by a large range of $(Nb/La)_{PM}$ for almost similar radiogenic $\epsilon_{Nd}(t)$. This range is observed in Dhuime et al. (2009) data but the increase in $(Nb/La)_{PM}$ is systematically associated with an increase in $\epsilon_{Nd}(t)$. For Spontang, two samples escape this tendency and are characterized by high $\epsilon_{Nd}(t)$ and low $(Nb/La)_{PM}$. This peculiar signature, observed to a lesser extent in all Spontang mafic rocks, may be

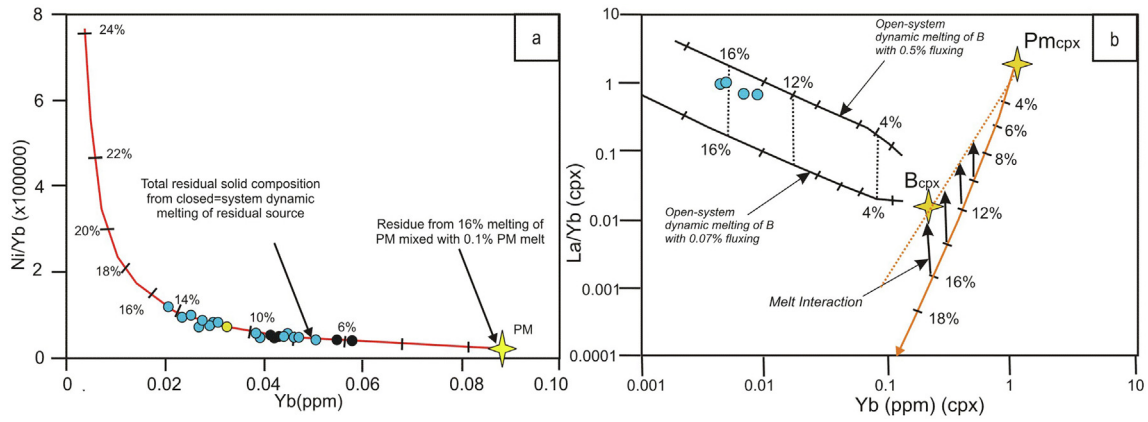


Fig. 18. Trace element melting models of the Spontang peridotites. a) Closed- and open-system dynamic melting of model source B are shown on (a) Ni/Yb versus Yb (ppm) and b) La/Yb versus Yb (ppm) bivariate diagram for clinopyroxene LA-ICPMS data.

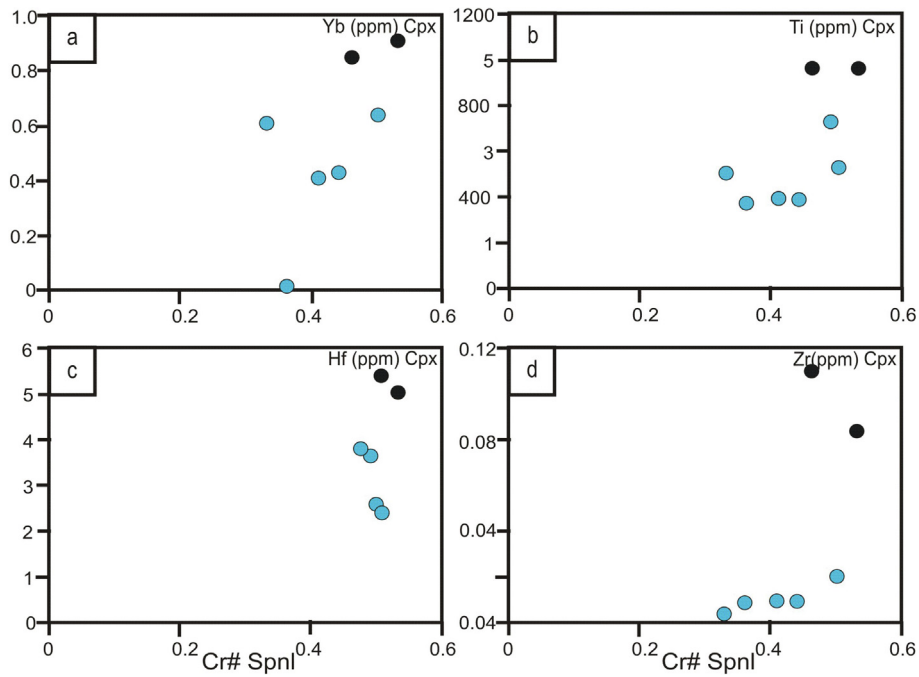


Fig. 19. Variations of spinel Cr# versus (a and b) Yb_N in Cpx and Opx (normalized by chondrite); (c and d) Ti in Cpx and Opx (ppm), (e and f) Hf in Cpx and Opx (ppm), (g and h) Zr in Cpx and Opx (ppm), (i and j) Nd in Cpx and Opx (ppm) in the Spontang peridotites.

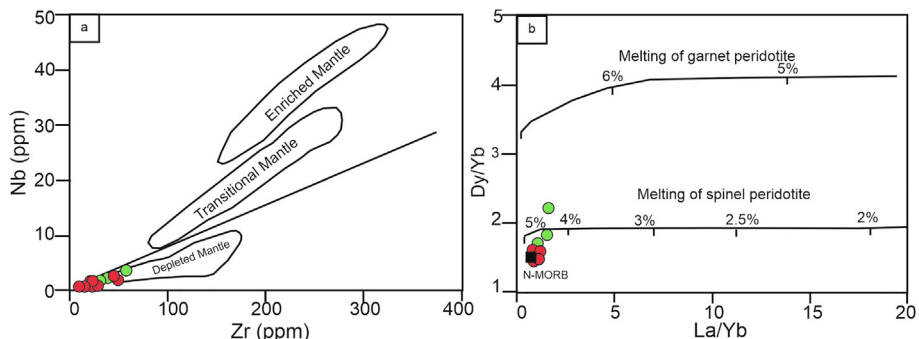


Fig. 20. Zr versus Nb diagram (after Geng et al., 2011) and (b) La/Yb versus Dy/Yb diagram (after Jung et al., 2006) for the Spontang mafic rocks. The normalizing values for N-MORB are from Sun and McDonough (1989).

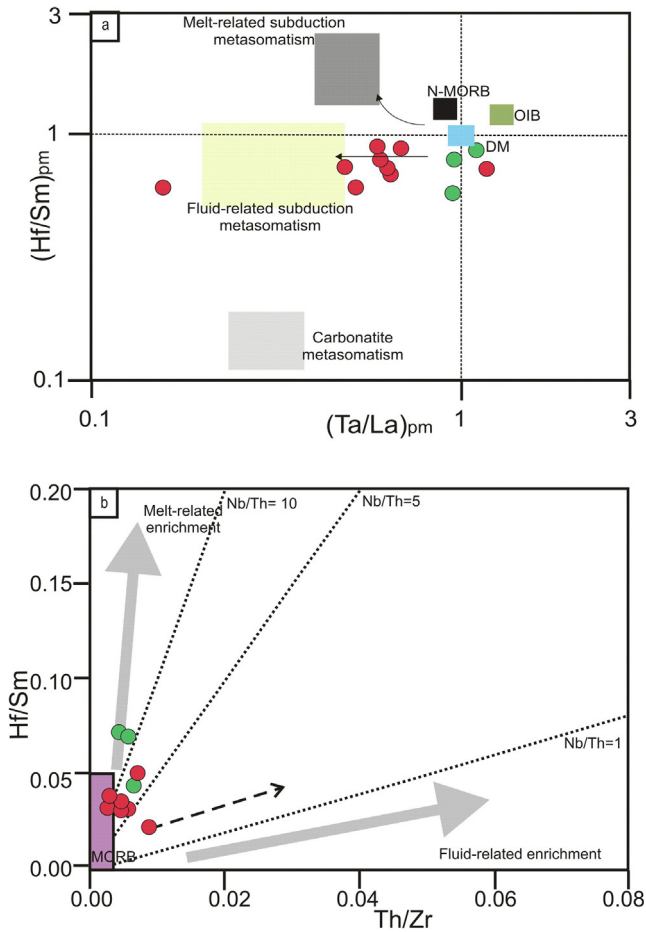


Fig. 21. a) $(Ta/La)_{PM}$ versus $(Hf/Sm)_{PM}$ (after Laflèche et al., 1998); b) Th/Zr versus Nb/Zr (Kepezhinskas et al., 1997) of the Spontang mafic samples.

related to the introduction of subduction-related fluids in the upper mantle source during the initiation of subduction. In this scenario, Nd isotopic composition may be buffered by the upper-mantle signature and Nb (and Ta) affected by metamorphic/magmatic processes happening during subduction.

6.6. Tectonic setting of the Spontang ophiolite

Peridotites in forearc settings are known to have a variety of origins, ranging from supra-subduction zone peridotites that equilibrated with hydrous fluids and melts derived from the subducting slab to previously formed abyssal peridotites trapped within a forearc region (Parkinson et al. 1992; Parkinson and Pearce, 1998; Pearce et al., 2000). This record of multiple tectonic settings may be attributed to complex melt-rock interaction (e.g. Elthon, 1992; Michibayashi et al., 2009; Dygert et al., 2016) and/or re-melting and re-crystallization processes that constituent mineral compositions through the ascending melts (Niu, et al., 1997). Ophiolitic rocks especially from the Ladakh area of the Indian Himalayas play a key role in reconstructing the timing and processes involved during Indo-Asia collision and deciphering the nature of the Neo-Tethyan oceanic crust and upper mantle (Hebert et al., 2012; Hu et al., 2016). Formation of the Spontang ophiolites although debated, is generally interpreted to represent supra-subduction tectonic settings (e.g. Reuber, 1986; Reuber et al., 1989, 1992; Aitchison et al., 2000; Pedersen et al., 2001; Aitchison and Davis, 2004; Maheo et al., 2004; Baxter et al., 2010; Clift et al., 2014). However, based on distinct whole-rock, trace and mineral chemistry of the studied samples presented above, formation is believed to have occurred in several distinct stages. The petrographic features as well as the major and mineral chemistry of the Spontang lherzolite and harzburgite domains are distinguished from each other in terms of the extent of mantle depletion, and metasomatic history, thereby defining a multi-stage evolution of the oceanic lithosphere formed during two

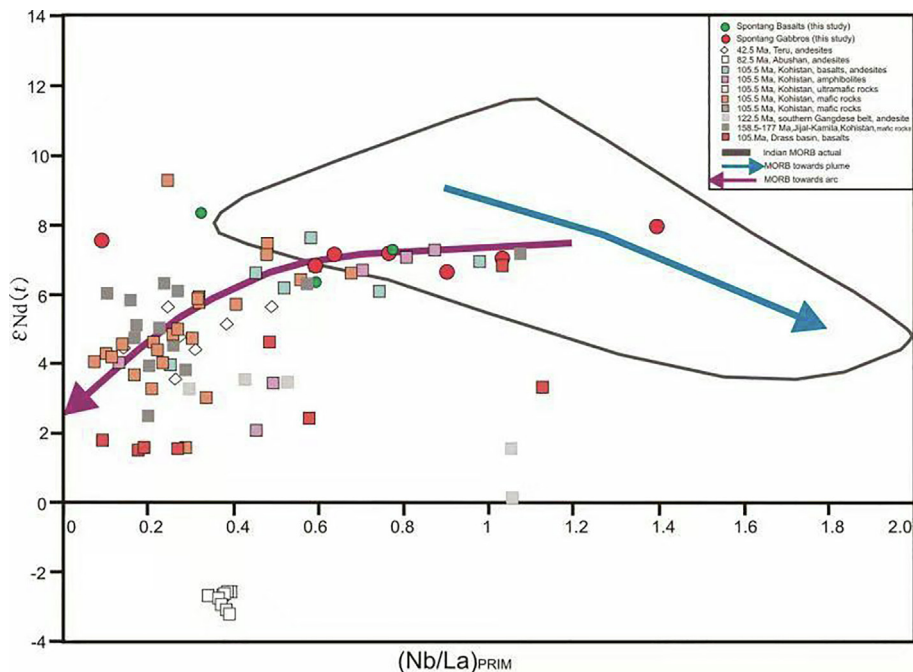


Fig. 22. $\epsilon Nd(t)$ vs $(Nb/La)_{PRIM}$ diagram for Spontang basalts and gabbros, superimposed on available isotopic data for mafic and ultramafic rocks from the ITSZ. Trace element data are normalized to the primitive mantle from Sun and McDonough (1989). All Nd data have end age corrected according to their measured or estimated emplacement ages. Present day Indian MORB domain is superimposed on the age-corrected data. The two arrows are illustrating the MORB toward Arc (double plain) and MORB toward Plume (dotted double) tendencies. References are same as in Fig. 8, except for Clift et al. (2000).

different episodes of lithosphere accretion from the convective mantle. The depleted lherzolites formed as products of 6%–8% partial melting of an anhydrous MOR-type melting beneath the mid-ocean ridge system and represents the first stage. This decompressional partial melting of a MOR mantle beneath a cold lithospheric lid at the spreading centre resulted in the lherzolites to be formed at high temperatures ($T_{\text{REE}} = 1216\text{ }^{\circ}\text{C}$) and probably reflect the original thermal state preserved just after their adiabatic decompression close to the estimated potential temperatures of the Phanerozoic mantle (approximately 1280–1350 $^{\circ}\text{C}$; Hezberg et al., 2010). As the subduction of the Neo Tethyan oceanic crust initiated in an intra-oceanic setting during the Middle Jurassic (177 Ma; Pedersen et al., 2001), the previously formed MOR- oceanic lithosphere was subsequently emplaced in the north-dipping subduction zone of the upper Neo-Tethyan plate. In this stage, the refractory harzburgites and dunites formed as residues after higher degrees of partial melting at lower temperatures ($T_{\text{REE}} = 1115\text{ }^{\circ}\text{C}$) of a depleted MORB source as a result of subduction initiation magmatism. Furthermore, metasomatism due to percolation of slab-derived fluids originating from the dehydrated serpentinites in the down going slab in the mantle wedge affected the host mantle rocks heterogeneously at all scales.

The Spontang massif exposes two groups of mafic rocks (viz. gabbros and basaltic units) and exhibit distinct geochemical differences i.e. MORB type of older age of 177 Ma (Pedersen et al., 2001) while the younger gabbros have primitive arc-related affinities of 136–133 Ma (Buckman et al., 2018) indicating the gabbroic magmatism with arc related affinity marks a second stage associated with the development of the Spong arc (Buckman et al., 2018). Field observations demonstrate a clear intrusive relationship between the mafic rocks and the harzburgites suggesting that accretion of the harzburgitic lithosphere must have occurred much earlier than the mafic magmatism. This inference is consistent with the Spontang harzburgite domain being located close to the crustal section within the Tethyan oceanic lithosphere as is observed in several other associated mantle – crustal units (e.g. Zedong ophiolite; Xiong et al., 2017). REE and isotopic abundances of the mafic samples analysed during the present study clearly exhibit elevated MREE-HREE abundances as well as elevated $\epsilon_{\text{Nd}}(t)$ and variable $^{87}\text{Sr}/^{86}\text{Sr}(t)$ displaying distinct N-MORB affinities and correspond to the older Jurassic ($\sim 177\text{ Ma}$; Pedersen et al., 2001) MORB-type Neotethyan oceanic crust associated with the earliest phase of subduction through which a younger intra-oceanic island arc (Spong arc) subsequently developed (Buckman et al., 2018). The mantle and crustal sections of the Spontang ophiolite were intruded by these younger gabbros with a distinct supra-subduction geochemical signature signifying an intra-oceanic subduction initiation and fore-arc spreading in $\sim 177\text{ Ma}$ oceanic crust, which led to the development of the Spong island-arc during the Cretaceous. Systematic enrichment in LILE's, $(\text{Ta}/\text{La})_{\text{PM}}$ and $(\text{Hf}/\text{Sm})_{\text{PM}}$ ratios for ultramafic rocks along with increase in $(\text{Nb}/\text{La})_{\text{PM}}$ versus $\epsilon_{\text{Nd}}(t)$ in the gabbros confirm their upper mantle affinity and clearly indicate that the mantle source of the mafic rocks was eventually metasomatized by subduction-related fluids during the Early Cretaceous.

7. Conclusions

- (1) The Spontang ophiolites expose ultramafic rocks consisting of depleted lherzolites, refractory harzburgites and dunites associated with mafic rocks (viz. gabbros and basalts) exposed along the Indus Tsangpo Suture Zone (closure of the Tethyan Ocean and collision of the Indian and Eurasian tectonic plates).

- (2) Petrological and geochemical data highlight the pristine characteristics of the Tethyan ocean lithosphere, with the Spontang peridotites transitioning from mid-ocean ridge spreading center to a subduction zone setting before closure of the Neo-Tethyan basin.
- (3) Distinct major, trace element and REE patterns (whole rock and mineral patterns) along with differing thermal conditions is consistent with the presence of both abyssal and SSZ signatures.
- (4) Initiation of subduction allows slab-derived fluids to interact with the mantle wedge, resulting in contrasted, transitional, geochemical signatures for the Spontang ophiolite.
- (5) Both ultramafic and mafic rocks studied here display isotopic and trace element signatures typical from N-MORB Neo-Tethyan oceanic crust generated first in an intra-oceanic setting to further evolve into SSZ.

Declaration of competing interest

The authors declare that they have no known competing financial interests or personal relationships that could have appeared to influence the work reported in this paper.

Acknowledgements

The authors thank the Head, Department of Geology and Interdisciplinary School of Science (IDSS), SPPU for providing necessary facilities. MKJ acknowledges the financial support received from Science Education and Research Board (SERB) and Department of Science and Technology (DST) by way of its Young Scientist Scheme (Ref. No. SR/FTP/ES-2/2014) Women's scientist scheme (Ref. No. SR/WOS-A/EA-14/2017). S. Mounic and A. Marquet respectively from Toulouse TIMS and ICPMS facilities. RT acknowledges a "Juan de la Cierva-formación" Fellowship (FJC2018-036729) granted by the Spanish Ministry of Science and Innovation and co-funded by the European Development Fund and the European Social Fund."

Appendix A. Supplementary data

Supplementary data to this article can be found online at <https://doi.org/10.1016/j.gsf.2021.101297>.

References

- Ahmad, T., Tanaka, T., Sachan, H.K., Asahara, Y., Islam, R., Khanna, P.P., 2008. Geochemical and isotopic constraints on the age and origin of the Nidar Ophiolitic Complex, Ladakh, India: implications for the Neo-Tethyan subduction along the Indus suture zone. *Tectonophysics* 451, 206–224.
- Aitchison, J.C., Ali, J.R., Davis, A.M., 2007. When and where did India and Asia collide? *J. Geophys. Res.* 112(B5).
- Aitchison, J.C., Davis, A.M., 2004. Evidence for the multiphase nature of the India-Asia collision from the Yarlung Tsangpo suture zone, Tibet. *Geol. Soc. Lon. Sp. Pl.* 226, 217–233.
- Aitchison, J.C., Davis, A.M., Liu, J., Luo, H., Malpas, J.G., McDermid, I.R., Wu, H., Ziabrev, S.V., Zhou, M.F., 2000. Remnants of a Cretaceous intra-oceanic subduction system within the Yarlung-Zangbo suture (southern Tibet). *Earth Planet. Sci. Lett.* 183, 231–244.
- Aldanmaz, E., Yaliniz, M.K., Guctekin, A., Goncuoglu, M.C., 2008. Geochemical characteristics of mafic lavas from the Neotethyan ophiolites in western Turkey: implications for heterogeneous source contribution during variable stages of ocean crust generation. *Geol. Mag.* 145, 37–54.
- Anonymous, 1972. Penrose field conference on ophiolites. *Geotimes* 17, 24–25.
- Arai, S., 1994a. Characterization of spinel peridotites by olivine-spinel compositional relationships: review and interpretation. *Chem. Geol.* 113, 191–204.
- Arai, S., 1994b. Compositional variation of olivine-chromian spinel in Mg-rich magmas as a guide to their residual spinel peridotites. *J. Vol. Geo. Res.* 59, 279–293.

- Barrat, J.A., Yamaguchi, A., Greenwood, R.C., Bohn, M., Cotton, J., Benoit, M., Franchi, I.A., 2007. The Stannern trend ecrites: contamination of Main-Group ecritic magmas by crustal partial melts. *Geochim. Cosmochim. Acta* 71, 4108–4124.
- Barth, M.G., Mason, P.R., Davies, G.R., Dijkstra, A.H., Drury, M.R., 2003. Geochemistry of the Othris ophiolite, Greece: evidence for refertilization? *J. Petrol.* 44 (10), 1759–1785.
- Bassoulet, J. P., Colchen, M., Juteau, T., Marcoux, J., Mascle, G., 1983. Geological studies in the Indus Zone of Ladakh (Himalayas). In *Stratigraphy and structure of Kashmir and Ladakh Himalaya*, 96–124.
- Baxter, A.T., Aitchison, J.C., Ali, J.R., Zybrev, S.V., 2010. Early Cretaceous radiolarians from the Spongtag massif, Ladakh, NW India: implications for Neo-Tethyan evolution. *J. Geol. Soc. Lond.* 167, 511–517.
- Bédard, É., Hébert, R., Guilmette, C., Lesage, G., Wang, C.S., Dostal, J., 2009. Petrology and geochemistry of the Saga and Sangsang ophiolitic massifs, Yarlung Zangbo Suture Zone, Southern Tibet: evidence for an arc-back-arc origin. *Lithos* 113, 48–67.
- Benoit, M., Ceuleneer, G., Polvé, M., 1999. The remelting of hydrothermally altered peridotite at mid-ocean ridges by intruding mantle diapirs. *Nature* 402, 514–518.
- Bignold, S.M., Treloar, P.J., 2003. Northward subduction of the Indian plate beneath the Kohistan Island Arc, Pakistan Himalaya: New evidence from isotope data. *J. Geol. Soc. Lond.* 160, 377–384.
- Bignold, S.M., Treloar, P.J., Petford, N., 2006. Changing sources of magma generation beneath intra-oceanic island arcs: An insight from the Juvenile Kohistan Island Arc, Pakistan Himalaya. *Chem. Geol.* 233, 46–74.
- Bodinier, J.L., Godard, M., 2004. Orogenic, ophiolitic and abyssal peridotites. In: Holland, H.D., Turekian, K.K. (Eds.), *Treatise on Geochemistry*. Elsevier, Amsterdam, pp. 103–170.
- Bodinier, J.L., Godard, M., 2007. Orogenic, ophiolitic and abyssal peridotites. In: Holland, H.D., Turekian, K.K. (Eds.), *Treatise on Geochemistry*. Elsevier, Amsterdam, pp. 1–73.
- Bonatti, E., Michael, P.J., 1989. Mantle peridotites from continental rifts to ocean basins to subduction zones. *Earth Planet. Sci. Lett.* 91, 297–311.
- Brey, G.P., Köhler, T., 1990. Geothermobarometry in four-phase lherzolites. II. New thermobarometers and practical assessment of existing thermobarometers. *J. Petrol.* 31, 1353–1378.
- Buckman, S., Aitchison, J.C., Nutman, A.P., Bennett, V.C., Saktura, W.M., Walsh, J.M., Kachovich, S., Hidaka, H., 2018. The Spongtag Massif in Ladakh, NW Himalaya: An Early Cretaceous record of spontaneous, intra-oceanic subduction initiation in the Neotethys. *Gondwana Res.* 63, 226–249.
- Burke, W.H., Denison, R.E., Hetherington, R.B., Koepnick, R.B., Nelson, H.F., Otto, H.F., 1982. Variation of seawater $^{87}\text{Sr}/^{86}\text{Sr}$ throughout Phanerozoic time. *Geology* 10, 516–519.
- Cawood, P.A., Kröner, A., Collins, W.J., Kusky, T.M., Mooney, W.D., Windley, B.F., 2009. Accretionary orogens through Earth history. *Geol. Soc. Lond. Sp. Pl.* 318, 1–36.
- Choi, S.H., Mukasa, S.B., Shervais, J.W., 2008. Initiation of Franciscan subduction along a large-offset fracture zone: Evidence from mantle peridotites, Stonyford, California. *Geology* 36, 595–598.
- Clift, P.D., Carter, A., Jonell, T.N., 2014. U-Pb dating of detrital zircon grains in the Paleocene Stumpata Formation, Tethyan Himalaya, Zaskar, India. *J. Asian Earth Sci.* 82, 80–89.
- Clift, P.D., Degnan, P.J., Hannigan, R., Blusztajn, J., 2000. Sedimentary and Geochemical Evolution of the Draf Forearc Basin, Indus Suture, Ladakh Himalaya, India. *Geol. Soc. Am. Bull.* 112, 450–466.
- Colchen, M., Reuber, I., Bassoulet, J.R., Bellier, J.R., Blondeau, A., Lys, M., de Wever, P., 1987. Données biostratigraphiques sur les mélanges ophiolitiques du Zaskar, Himalaya du Ladakh. *Comptes rendus de l'Académie des Sci. Paris*, 305, 403–406.
- Colchen, M., Reuber, I., 1986. Les mélanges ophiolitiques du Zaskar. Himalaya du Ladakh. *Comptes rendus de l'Académie des Sci. Paris* 303, 719–724.
- Coleman, R. G., 1977. Ophiolites, Ancient Oceanic Lithosphere? In: Wyllie, P. J. (Ed.), *Springer-Verlag*, New York, p. 229. Corfield, R. I., Searle, M. P., 2000. Crustal shortening estimates across the north Indian continental margin, Ladakh, NW India. *Geol. Soc. Lond. Sp. Pl.* 170, 395–410.
- Corfield, R.I., Searle, M.P., Green, O.R., 1999. Photang thrust sheet—An accretionary complex structurally below the Spontang ophiolite constraining timing and tectonic environment of ophiolite obduction, Ladakh Himalaya, NW India. *J. Geol. Soc. Lond.* 156, 1031–1044.
- Corfield, R.I., Searle, M.P., Pedersen, R.B., 2001. Tectonic Setting, Origin, and Obduction History of the Spontang Ophiolite, Ladakh Himalaya, NW India. *J. Geol.* 109, 715–736.
- Cox, K.G., Bell, J.D., Pankhurst, R.J., 1979. *The Interpretation of Igneous Rocks*. (Eds.), George Allen and Unwin, London, 1–450.
- de Sigoyer, J., Guillot, S., Lardeaux, J.M., Mascle, G., 1997. Glaucofan bearing eclogites in the Tso Moriri dome eastern Ladakh NW Himalaya. *Eur. J. Mineral.* 9, 1073–1083.
- Dewey, J.F., Bird, J.M., 1971. Origin and emplacement of the ophiolite suite: Appalachian ophiolites in Newfoundland. *J. Geophys. Res.* 76, 3179–3206.
- Dhuime, B., Bosch, D., Garrido, C.J., Bodinier, J.L., Bruguier, O., Hussain, S.S., Dawood, H., 2009. Geochemical architecture of the lower- to middle-crustal section of A PALEO-ISLAND arc (Kohistan Complex, Jijal-Kamila Area, Northern Pakistan): implications for the evolution of an oceanic subduction zone. *J. Petrol.* 50, 531–569.
- Dhuime, B., Bosch, D., Bodinier, J.L., Garrido, C.J., Bruguier, O., Hussain, S.S., Dawood, H., 2007. Multistage evolution of the Jijal Ultramafic-Mafic Complex (Kohistan, N Pakistan): implications for building the roots of island arcs. *Earth Planet. Sci. Lett.* 261, 179–200.
- Dilek, Y., Flower, M.F., 2003. Arc-trench rollback and forearc accretion: 2. A model template for ophiolites in Albania, Cyprus, and Oman. *Geol. Soc. Lond. Spec. Pub.* 218, 43–68.
- Dilek, Y., Furnes, H., 2011. Ophiolite genesis and global tectonics: Geochemical and tectonic fingerprinting of ancient oceanic lithosphere. *Geol. Soc. Am. Bull.* 123, 387–411.
- Dilek, Y., Furnes, H., Shallo, M., 2007. Suprasubduction zone ophiolite formation along the periphery of Mesozoic Gondwana. *Gondwana Res.* 11, 453–475.
- Dilek, Y., Morishita, T., 2009. Melt migration and upper mantle evolution during incipient arc construction: Jurassic Eastern Mirdita ophiolite, Albania. *Island Arc* 18, 551–554.
- Dilek, Y., Thy, P., Hacker, B., Grundvig, S., 1999. Structure and petrology of Tauride ophiolites and mafic dike intrusions (Turkey): Implications for the Neotethyan ocean. *Geol. Soc. Am. Bull.* 111, 1192–1216.
- Dubois-Côté, V., Hébert, R., Dupuis, C., Wang, C.S., Li, Y.L., Dostal, J., 2005. Petrological and geochemical evidence for the origin of the Yarlung Zangbo ophiolites, southern Tibet. *Chem. Geol.* 214, 265–286.
- Dupuis, C., Hébert, R., Dubois-Côté, V., Guilmette, C., Wang, C.S., Li, Y.L., Li, Z.J., 2005. The Yarlung Zangbo Suture Zone ophiolitic mélange (southern Tibet): new insights from geochemistry of ultramafic rocks. *J. Asian Earth Sci.* 25, 937–960.
- Dyger, N., Liang, Y., Kelemen, P.B., 2016. Formation of plagioclase lherzolite and associated dunite-harzburgite-lherzolite sequences by multiple episodes of melt percolation and melt-rock reaction: an example from the Trinity Ophiolite, California, USA. *J. Petrol.* 57, 815–838.
- Eiler, J.M., Schiano, P., Kitchen, N., Stolper, E.M., 2000. Oxygen-isotope evidence for recycled crust in the sources of mid-ocean-ridge basalts. *Nature* 403, 530–534.
- Eiler, J.M., Schiano, P., Valley, J.W., Kita, N.T., Stolper, E.M., 2007. Oxygen-isotope and trace element constraints on the origins of silica-rich melts in the subarc mantle. *Geochem. Geophys. Geosys.* 8. <https://doi.org/10.1029/2006GC001503>.
- Elthon, D., 1992. Chemical trends in abyssal peridotites: refertilization of depleted suboceanic mantle. *J. Geophys. Res.* 97, 9015–9025.
- Fabries, I., 1979. Spinel-olivine geothermometry in peridotites from ultramafic complexes. *Contrib. Mineral. Petrol.* 69, 329–36.
- Foley, S.F., Prelevic, D., Rehfeldt, T., Jacob, D.E., 2013. Minor and trace elements in olivines as probes into early igneous and mantle melting processes. *Earth Planet. Sci. Lett.* 363, 181–191.
- Fuchs, G., 1979. On the geology of western Ladakh. *Jahrb. Geol. Bundesanst.* 122, 513–540.
- Fuchs, G., 1982. The geology of western Zaskar. *Jahrb. Geol. Bundesanst.* 125, 1–50.
- Gansser, A., 1977. The great suture zone between Himalaya and Tibet: A Preliminary Account. *CNRS, Colloque Internat* 268, 1881–1892. Gansser, A., 1980. The significance of the Himalayan suture zone. *Tectonophysics*. 62, 37–52.
- Gasparik, T., 1987. Orthopyroxene thermometry in simple and complex systems. *Contrib. Mineral. Petrol.* 96, 357–370.
- Ghosh, B., Bandyopadhyay, D., Morishita, T., 2017. Andaman-Nicobar Ophiolites, India: origin, evolution and emplacement. *Geol. Soc. Lond.* 47, 95–110.
- Girardeau, J., Marcoux, J., Fourcade, E., Bassoulet, J.P., Youking, T., 1985a. Xainxa ultramafic rocks, central Tibet, China: Tectonic environment and geodynamic significance. *Geology*. 13, 330–333.
- Girardeau, J., Mercier, J.C., Yougong, Z., 1985b. Origin of the Xigaze ophiolite, Yarlung Zangbo suture zone, southern Tibet. *Tectonophysics*. 119, 407–433.
- Godard, M., Lagabrielle, Y., Alard, O., Harvey, J., 2008. Geochemistry of the highly depleted peridotites drilled at ODP Sites 1272 and 1274 (Fifteen-Twenty Fracture Zone, Mid-Atlantic Ridge): Implications for mantle dynamics beneath a slow spreading ridge. *Earth Planet. Sci. Lett.* 267, 410–425.
- Göpel, C., Allègre, C.J., Xu, R.H., 1984. Lead isotopic study of the Xigaze ophiolite (Tibet): the problem of the relationship between magmatites (gabbros, dolerites, lavas) and tectonites (harzburgites). *Earth Planet. Sci. Lett.* 69, 301–310.
- Hart, S.R., Zindler, A., 1986. In search of a bulk-Earth composition. *Chem. Geol.* 57, 247–267.
- Hébert, R., Bezard, R., Guilmette, C., Dostal, J., Wang, C.S., Liu, Z.F., 2012. The Indus-Yarlung Zangbo ophiolites from Nanga Parbat to Namche Barwa syntaxes, southern Tibet: first synthesis of petrology, geochemistry, and geochronology with incidences on geodynamic reconstructions of Neo-Tethys. *Gondwana Res.* 22, 377–397.
- Hellebrand, E., Snow, J.E., Hoppe, P., Hofmann, A., 2002. Garnet field melting and late stage refertilization in 'residual' abyssal peridotites from the Central Indian Ridge. *J. Petrol.* 43, 2305–2338.
- Hellebrand, E., Snow, J.E., Dick, H.J.B., Hofmann, A.W., 2001. Coupled major and trace elements as indicator of the extent of melting in mid-ocean-ridge peridotites. *Nature* 410, 677–681.
- Hezberg, C., Condie, K., Korenaga, J., 2010. Thermal history of the Earth and its petrological expression. *Earth Planet. Sci. Lett.* 292, 79–88.
- Hofmann, A.W., 1988. Chemical differentiation of the Earth: the relationship between mantle, continental crust, and oceanic crust. *Earth Planet. Sci. Lett.* 90, 297–314.
- Honegger, K., Dietrich, V., Frank, W., Gansser, A., Thöni, M., Trommsdorff, V., 1982. Magmatism and metamorphism in the Ladakh Himalayas (the Indus-Tsangpo suture zone). *Earth Planet. Sci. Lett.* 60, 253–292.
- Hu, X., Garzanti, E., Wang, J., Huang, W., An, W., Webb, A., 2016. The timing of India-Asia collision onset—Facts, theories, controversies. *Earth-Sci. Rev.* 160, 264–299.

- Ishikawa, A., Kaneko, Y., Kadarusman, A., Ota, T., 2007. Multiple generations of forearc mafic-ultramafic rocks in the Timor-Tanimbar ophiolite, eastern Indonesia. *Gondwana Res.* 11, 200–217.
- Jan, M.Q., Windley, B.F., Khan, A., 1985. The Waziristan ophiolite, Pakistan: general geology and chemistry of chromite and associated phases. *Eco. Geol.* 80, 294–306.
- Johnson, K.T.M., Dick, H.J.B., 1992. Open system melting and temporal and spatial variation of peridotite and basalt at the Atlantis II fracture zone. *J. Geophys. Res.* 97, 9219–9241.
- Johnson, K.T.M., Dick, H.J.B., Shimizu, N., 1990. Melting in the oceanic upper mantle: an ion microprobe study of diopsides in abyssal peridotites. *J. Geophys. Res.* 95, 2661–2678.
- Jonnalagadda, M.K., Karmalkar, N.R., Benoit, M., Gregoire, M., Duraiswami, R.A., Harshe, S., Kamble, S., 2019. Compositional variations of chromian spinels from peridotites of the Spontang ophiolite complex, Ladakh, NW Himalayas, India: petrogenetic implications. *Geosci. J.* 23, 895–915.
- Jung, C., Jung, S., Hoffer, E., Berndt, J., 2006. Petrogenesis of Tertiary Mafic Alkaline Magmas in the Hoheifel, Germany. *J. Petrol.* 47, 1637–1671.
- Juteau, T., Berger, E., and Cannat, M., 1990. Serpentinized, residual mantle peridotites from the M.A.R. median valley, ODP hole 670A (21° 10'N, 45° 02'W): primary mineralogy and geothermometry. In: Detrick, R., Honnorez, J., Bryan, W.B., and Juteau, T., (Eds.), *Proc. Ocean Drill. Prog. Sci. Res.* 106, 27–45.
- Kakar, M.I., Mahmood, K., Kerr, A.C., Khan, M., 2013a. Petrology of the mantle rocks from the Muslim Bagh Ophiolite, Balochistan, Pakistan. *J. Him. Earth Sci.* 46 (2), 101–112.
- Kakar, M.I., Mahmood, K., Khan, M., Kasi, A.K., Manan, R.A., 2013b. Petrology and geochemistry of gabbros from the Muslim Bagh Ophiolite: implications for their petrogenesis and tectonic setting. *J. Him. Earth Sci.* 46 (1), 19–30.
- Kang, Z.Q., Xu, J.F., Wilde, S.A., Feng, Z.H., Chen, J.L., Wang, B.D., Fu, W.C., Pan, H.B., 2014. Geochronology and Geochemistry of the Sangri Group Volcanic Rocks, Southern Lhasa Terrane: Implications for the Early Subduction History of the Neo-Tethys and Gangdese Magmatic Arc. *Lithos* 200, 157–168.
- Kelemen, P.B., and Sonnenfeld, M.D., 1983. Stratigraphy, structure, petrology and local tectonics, Central Ladakh, NW Himalaya. *Schweizerische Mineralogische und Petrographische Mitteilungen* 63, 267–287.
- Kelemen, P.B., Dick, H.J., Quick, J.E., 1992. Formation of harzburgite by pervasive melt/rock reaction in the upper mantle. *Nature* 358, 635–641.
- Kepezhinskas, P., McDermott, F., Defant, M.J., Hochstaedter, A., Drummond, M.S., Hawkesworth, C.J., Bellon, H., 1997. Trace element and Sr-Nd-Pb isotopic constraints on a three-component model of Kamchatka Arc petrogenesis. *Geochim. Cosmochim. Acta* 61, 577–600.
- Khan, M.A., Stern, R.J., Hole, M.J., Windley, B.F., 1997. Geochemical and isotopic constraints on subduction polarity, magma sources, and palaeogeography of the Kohistan intra-oceanic arc, northern Pakistan Himalaya. *J. Geol. Soc. Lon.* 154, 935–946.
- Khan, S.D., Stern, R.J., Manton, M.I., Copeland, P., Kimura, J.I., Khan, M.A., 2004. Age, geochemical and Sr-Nd-Pb isotopic constraints for mantle source characteristics and petrogenesis of Teru Volcanics, Northern Kohistan Terrane, Pakistan. *Tectonophysics* 393, 263–280.
- Kostopoulos, D.K., 1991. Melting of the shallow upper mantle: a new perspective. *J. Petrol.* 32, 671–699.
- Lafliche, M.R.L., Camiré, G., Jenner, G.A., 1998. Geochemistry of post-Acadian, Carboniferous continental intraplate basalts from the Maritimes Basin, Magdalen Islands, Québec, Canada. *Chem. Geol.* 148, 115–136.
- Lagabriele, Y., Guivel, C., Maury, R.C., Bourgeois, J., Fourcade, S., Martin, H., 2000. Magmatic-tectonic effects of high thermal regime at the site of active ridge subduction: the Chile Triple Junction model. *Tectonophysics* 326 (3–4), 255–268.
- Lanphere, M.A., Coleman, R.G., Hopson, C.A., 1981. Sr isotopic tracer study of the Samail ophiolite, Oman. *J. Geophys. Res.* 86, 2709–2720.
- Le Bas, M.J., Le Maitre, R.W., Streckeisen, A., Zanettin, B., 1986. A chemical classification of volcanic rocks based on the total alkali-silica diagram. *J. Petrol.* 27, 745–750.
- Le Fort, P., 1975. Himalayas: the collided range. Present knowledge of the continental arc. *Am. J. Sci.* 275, 1–44.
- Le Roux, V., Nielsen, S.G., Sun, C., Yao, L., 2016. Dating layered websterite formation in the lithospheric mantle. *Earth Planet. Sci. Lett.* 454, 103–112.
- Lee, H.Y., Chung, S.L., Ji, J., Qian, Q., Gallet, S., Lo, C.H., Lee, T.Y., Zhang, Q., 2012. Geochemical and Sr-Nd isotopic constraints on the genesis of the Cenozoic Linzong volcanic successions, southern Tibet. *J. Asian Earth Sci.* 53, 96–114.
- Li, Q., Xia, B., Li, J., Xia, L., Huang, Q., Xia, Z., 2015. Mineral chemistry and geochemistry of peridotites from the Zedang and Luobusa ophiolites, Tibet: Implications for the evolution of the Neo-Tethys. *J. Earth Sci.* 26, 893–910.
- Liang, Y., Sun, C., Yao, L., 2013. A REE-in-two-pyroxene thermometer for mafic and ultramafic rocks. *Geochim. Cosmochim. Acta* 102, 246–260.
- Lippard, S.J., 1986. The ophiolite of northern Oman. *Geol. Soc. Lon. Mem.* 11, 178.
- Maheo, G., Bertrand, H., Guillot, S., Villa, I.M., Keller, F., Capiez, P., 2004. The South Ladakh ophiolites (NW Himalaya, India): an intra-oceanic tholeiitic arc origin with implication for the closure of the Neo-Tethys. *Chem. Geol.* 203, 273–303.
- Mahoney, J.J., Frei, R., Tejada, M.L.G., Mo, X.X., Leat, P.T., Nägler, T.F., 1998. Tracing the Indian Ocean mantle domain through time: isotopic results from old West Indian, East Tethyan, and South Pacific seafloor. *J. Petrol.* 39, 1285–1306.
- Mahoney, J.J., Graham, D.W., Christie, D.M., Johnson, K.T.M., Hall, L.S., Vonderhaar, D.L., 2002. Between a hotspot and a cold spot: isotopic variation in the Southeast Indian Ridge asthenosphere, 86 E–118 E. *J. Petrol.* 43, 1155–1176.
- McCulloch, M.T., Gamble, J.A., 1991. Geochemical and geodynamical constraints on subduction zone magmatism. *Earth Planet. Sci. Lett.* 102, 358–374.
- McCulloch, M.T., Gregory, R.T., Wasserburg, G.J., Taylor Jr, H.P., 1981. Sm-Nd, Rb-Sr, and 180/160 isotopic systematics in an oceanic crustal section: Evidence from the Samail Ophiolite. *J. Geophys. Res.* 86, 2721–2735.
- McDermid, I.R., Aitchison, J.C., Davis, A.M., Harrison, T.M., Grove, M., 2002. The Zedong terrane: a Late Jurassic intra-oceanic magmatic arc within the Yarlung-Tsangpo suture zone, southeastern Tibet. *Chem. Geol.* 187, 267–277.
- Michibayashi, K., Ohara, Y., Stern, R.J., Fryer, P., Kimura, J.I., Tasaka, M., Harigane, Y., Ishii, T., 2009. Peridotites from a ductile shear zone within back-arc lithospheric mantle, southern Mariana Trench: Results of a Shinkai 6500 dive. *Geochem. Geophys. Res.* 10 (5).
- Miller, C., Thöni, M., Frank, W., Schuster, R., Melcher, F., Meisel, T., Zanetti, A., 2003. Geochemistry and tectonomagmatic affinity of the Yungbwa ophiolite, SW Tibet. *Lithos* 66, 155–172.
- Miyashiro, A., 1974. Volcanic rock series in island arcs and active continental margins. *Am. J. Sci.* 274, 321–355.
- Molnar, P., Tapponnier, P., 1975. Cenozoic tectonics of Asia: effects of a continental collision. *Science* 189, 419–426.
- Morimoto, N., Fabries, J., Ferguson, A.K., 1988. Pyroxene nomenclature. *Mineral. Petrol.* 39, 55–76.
- Morishita, T., Dilek, Y., Shallo, M., Tamura, A., Arai, S., 2011. Insight into the uppermost mantle section of a maturing arc: The Eastern Mirdita ophiolite, Albania. *Lithos* 124, 215–226.
- Nicolas, A., 1989. Structures of Ophiolites and Dynamics of Oceanic Lithosphere. Kluwer Academic Publishers, Dordrecht, p. 320.
- Nicolas, A., Girardeau, J., Marcoux, J., Dupre, B., Xibin, W., Yougong, C., Yougong, Z.H., Xuchang, X., 1981. The Xigaze ophiolite (Tibet): a peculiar oceanic lithosphere. *Nature* 294, 414–417.
- Nimis, P., Grütter, H., 2010. Internally consistent geothermometers for garnet peridotites and pyroxenites. *Contrib. Mineral. Petrol.* 159, 411–427.
- Niu, Y., 2004. Bulk-rock major and trace element compositions of abyssal peridotites: implications for mantle melting, melt extraction and post-melting processes beneath mid-ocean ridges. *J. Petrol.* 45, 2423–2458.
- Niu, Y., Langmuir, C.H., Kinzler, R.J., 1997. The origin of abyssal peridotites: a new perspective. *Earth Planet. Sci. Lett.* 152, 251–265.
- Nonnotte, P., Ceuleneer, G., Benoit, M., 2005. Genesis of andesitic-boninitic magmas at mid-ocean ridges by melting of hydrated peridotites: geochemical evidence from DSDP Site 334 gabbroanites. *Earth Planet. Sci. Lett.* 236, 632–653.
- Ohara, Y., Ishii, T., 1998. Peridotites from the southern Mariana forearc: heterogeneous fluid supply in the mantle wedge. *Island Arc* 7, 541–558.
- Ozawa, K., 1994. Melting and melt segregation in the mantle wedge above a subduction zone: evidence from the chromite-bearing peridotites of the Miyamori Ophiolite Complex, northeastern Japan. *J. Petrol.* 35, 647–678.
- Pagé, P., Bédard, J.H., Schroetter, J.-M., Tremblay, A., 2008. Mantle petrology and mineralogy of the Thetford Mines ophiolite complex. *Lithos* 100, 255–292.
- Pal, T., Chakraborty, P.P., Gupta, T.D., Singh, C.D., 2003. Geodynamic evolution of the outer-arc-forearc belt in the Andaman Islands, the central part of the Burma-Java subduction complex. *Geol. Mag.* 140, 289–307.
- Parkinson, I., Pearce, J.A., Thirlwall, M.E.A., Johnson, K.T.M., Ingram, G., 1992. Trace element geochemistry of peridotites from the Izu-Bonin-Mariana forearc, Leg 125. *Proc. Ocean Drill. Prog. Sci. Res.* 125, 487–506.
- Parkinson, I.J., Pearce, J.A., 1998. Peridotites from the Izu-Bonin-Mariana forearc (ODP Leg 125): evidence for mantle melting and melt-mantle interactions in a supra-subduction zone setting. *J. Petrol.* 39, 1577–1618.
- Paulick, H., Bach, W., Godard, M., De Hoog, J.C.M., Suhr, G., Harvey, J., 2006. Geochemistry of abyssal peridotites (Mid-Atlantic Ridge, 15° 20' N, ODP Leg 209): implications for fluid/rock interaction in slow spreading environments. *Chem. Geol.* 234, 179–210.
- Pearce, J.A., 2003. Supra-subduction zone ophiolites: The search for modern analogues. *Sp. Papers-Geol. Soc. Am.*, 269–294.
- Pearce, J.A., 2005. Mantle preconditioning by melt extraction during flow: Theory and petrogenetic implications. *J. Petrol.* 46, 973–997.
- Pearce, J.A., 2008. Geochemical fingerprinting of oceanic basalts with applications to ophiolite classification and the search for Archean oceanic crust. *Lithos* 100, 14–48.
- Pearce, J.A., Cann, J.R., 1973. Tectonic setting of basic volcanic rocks determined using trace element analyses. *Earth Planet. Sci. Lett.* 19, 290–300.
- Pearce, J.A., Norry, M.J., 1979. Petrogenetic implications of Ti, Zr, Y, and Nb variations in volcanic rocks. *Contrib. Mineral. Petrol.* 69, 33–47.
- Pearce, J.A., Peate, D.W., 1995. Tectonic implications of the composition of volcanic arc magmas. *Ann. Rev. Earth Pl. Sc.* 23, 251–286.
- Pearce, J.A., Stern, R.J., 2006. Origin of back-arc basin magmas: trace element and isotope perspectives. *American Geophysical Union* 166, 63.
- Pearce, J.A., Barker, P.F., Edwards, S.J., Parkinson, I.J., Leat, P.T., 2000. Geochemistry and tectonic significance of peridotites from the South Sandwich arc-basin system, South Atlantic. *Contrib. Mineral. Petrol.* 139, 36–53.
- Pearce, J.A., Robinson, P.T., 2010. The Troodos ophiolite complex probably formed in a subduction initiation, slab edge setting. *Gondwana Res.* 18, 60–81.
- Pearce, J.A., van der Laan, S.R., Arculus, R.J., Murton, B.J., Ishii, T., Peate, D.W., Parkinson, I.J., 1992. Boninite and harzburgite from Leg 125 (Bonin-Mariana forearc): A case study of magma genesis during the initial stages of subduction. *Proc. Ocean Drill. Prog. Sci. Res.* 125, 623–659.
- Pedersen, R.B., Searle, M.P., Corfield, R.I., 2001. U-Pb Zircon ages from the Spontang Ophiolite, Ladakh Himalaya. *J. Geol. Soc. Lon.* 158, 513–520.
- Radhakrishna, T., Rao, V.D., Murali, A.V., 1984. Geochemistry of Dras Volcanics and the evolution of the Indus Suture ophiolites. *Tectonophysics* 108, 135–153.

- Radhakrishna, T., Rao, V.D., Murali, A.V., 1987. Geochemistry and petrogenesis of ultramafic and mafic plutonic rocks of the Dras ophiolitic melange, Indus suture (northwest Himalaya). *Earth Planet. Sci. Lett.* 82 (1–2), 136–144.
- Reibel, G., Reuber, I., 1982. La klippe ophiolitique de Spongtang-Photaksär (Himalaya du Ladakh); une ophiolite sans cumulais. *Comptes rendus de l'Académie des Sciences, Paris.* 294, 557–562.
- Reuber, I., 1986. Geometry of accretion and oceanic thrusting of the Spontang Ophiolite, Ladakh Himalaya. *Nature* 321, 592–596.
- Reuber, I., Colchen, M., Mevel, C., 1992. The Spontang ophiolite and ophiolitic mélanges of the Zaskar, N.W. Himalaya, tracing the evolution of the closing Tethys in the upper Cretaceous to the Early Tertiary. In: Sinha, A.K. (Ed.), *Himalayan Orogen and Global Tectonics*. A.A. Balkema, Rotterdam, p. 31.
- Reuber, I., Montigny, R., Thuizai, R., Heitz, A., 1989. K-Ar ages of ophiolites and arc volcanics of the Indus suture zone: clues on the early evolution of the Neo-Tethys. *Ecl. Geol. Hel.* 82, 699–715.
- Robertson, A.H.F., 2000. Formation of melanges in the Indus suture zone, Ladakh Himalaya by successive subduction-related, collisional and post-collisional processes during late Mesozoic-late Tertiary time. *Geol. Soc. Lon. Spec. Pub.* 170, 333–374.
- Saha, D., 2010. Palaeoproterozoic dismembered ophiolites in Kandra Nappe Complex, south India. *Asia Oceania Geos. Soc.* 10, 5–9.
- Sarwar, G., 1992. Tectonic setting of the Bela Ophiolites, southern Pakistan. *Tectonophy* 207, 359–381.
- Searle, M.P., 1986. Structural evolution and sequence of thrusting in the High Himalayan, Tibetan–Tethys and Indus suture zones of Zaskar and Ladakh, Western Himalaya. *J. Struc. Geol.* 8, 923–936.
- Seyler, M., Lorand, J.P., Dick, H.J., Drouin, M., 2007. Pervasive melt percolation reactions in ultra-depleted refractory harzburgites at the Mid-Atlantic Ridge, 15° 20' N: ODP Hole 1274A. *Contrib. Mineral. Petrol.* 153, 30.
- Sheraton, J.W., 1984. Chemical changes associated with high-grade metamorphism of mafic rocks in the East Antarctic Shield. *Chem. Geol.* 47, 135–157.
- Shervais, J.W., 2001. Birth, death, and resurrection: The life cycle of suprasubduction zone ophiolites. *Geochem. Geophys. Geosys.*, 2
- Sinha, A.K., Mishra, M., 1994. The existence of oceanic islands in the Neotethys: Evidence from Ladakh Himalaya, India. *Curr. Sci.*, 721–727
- Snow, J.E., Dick, H.J., 1995. Pervasive magnesium loss by marine weathering of peridotite. *Geochim. Cosmochim. Acta* 59, 4219–4236.
- Spooner, E.T.C., 1976. The strontium isotopic composition of seawater, and seawater-oceanic crust interaction. *Earth Planet. Sci. Lett.* 31, 167–174.
- Srikantia, S.V., Razdan, M.L., 1981. Shilakong ophiolite nappe of Zaskar Mountains, Ladakh Himalaya. *J. Geol. Soc. Ind.* 22, 227–234.
- Sun, S.S., McDonough, W.F., 1989. Chemical and isotopic systematics of oceanic basalts: implications for mantle composition and processes. In: Saunders, A.D., Norry, M.J. (Eds.), *Magmatism in Ocean Basins*. Geol. Soc. Spec. Publ., London, pp. 313–345.
- Thompson, G., 1973. A geochemical study of the low-temperature interaction of seawater and oceanic igneous rocks. *EOS. Trans. Am. Geophys. Uni.* 54, 1015–1019.
- Tilhac, R., Ceuleneer, G., Griffin, W.L., O'Reilly, S.Y., Pearson, N.J., Benoit, M., Henry, H., Girardeau, J., Grégoire, M., 2016. Primitive arc magmatism and delamination: petrology and geochemistry of Pyroxenites from the Cabo Ortegal Complex, Spain. *J. Petrol.* 57, 1921–1954.
- Uysal, I., Ersoy, E.Y., Karsli, O., Dilek, Y., Sadıklar, M.B., Ottley, C.J., Tiepolo, M., Meisel, T., 2012. Coexistence of abyssal and ultra-depleted SSZ type mantle peridotites in a Neo-Tethyan Ophiolite in SW Turkey: Constraints from mineral composition, whole-rock geochemistry (major–trace–REE–PGE), and Re–Os isotope systematics. *Lithos* 132, 50–69.
- Uysal, I., Kaliwoda, M., Karsli, O., Tarkian, M., Sadıklar, M.B., Ottley, C.J., 2007. Compositional variations as a result of partial melting and melt–peridotite interaction in an upper mantle section from the Ortaca area, southwestern Turkey. *Can. Mineral.* 45, 1471–1493.
- Van Achterbergh, E., Ryan, C.G., Jackson, S.E., Griffin, W.L., 2001. Data reduction software for LA-ICP-MS: appendix; In: Sylvester, P.J. (Eds.), *Mineralogical Association of Canada Short Course Series*, Ottawa, Ontario, Canada. 29, 239–243.
- Warren, J.M., 2016. Global variations in abyssal peridotite compositions. *Lithos* 248, 193–219.
- Woodhead, J.D., Hergt, J.M., Davidson, J.P., Eggins, S.M., 2001. Hafnium isotope evidence for 'conservative' element mobility during subduction zone processes. *Earth Planet. Sci. Lett.* 192, 331–346.
- Xia, B., Yu, H.X., Chen, G.W., Qi, L., Zhao, T.P., Zhou, M.F., 2003. Geochemistry and tectonic environment of the Dagzhuka ophiolite in the Yarlung-Zangbo suture zone, Tibet. *Geochem. J.* 37, 311–324.
- Xiong, Q., Henry, H., Griffin, W.L., Zheng, J.P., Satsukawa, T., Pearson, N.J., O'Reilly, S. Y., 2017. High- and low-Cr chromite and dunite in a Tibetan ophiolite: evolution from mature subduction system to incipient forearc in the Neo-Tethyan Ocean. *Contrib. Mineral. Petrol.* 172, 45.
- Xu, X., O'Reilly, S.Y., Griffin, W.L., Zhou, X., 2003. Enrichment of upper mantle peridotite: petrological, trace element and isotopic evidence in xenoliths from SE China. *Chem. Geol.* 198, 163–188.
- Xu, Y.G., 2014. Recycled oceanic crust in the source of 90–40 Ma basalts in North and Northeast China: evidence, provenance and significance. *Geochim. Cosmochim. Acta* 143, 49–67.
- Zaigham, N.A., Mallick, K.A., 2000. Bela ophiolite zone of southern Pakistan: Tectonic setting and associated mineral deposits. *Geol. Soc. of Am. Bull.* 112, 478–489.
- Zhou, M.F., Robinson, P.T., Malpas, J., Edwards, S.J., Qi, L., 2005. REE and PGE geochemical constraints on the formation of dunites in the Luobusa Ophiolite, southern Tibet. *J. Petrol.* 46, 615–639.
- Zhou, M.F., Sun, M., Keays, R.R., Kerrich, R.W., 1998. Controls on platinum-group elemental distributions of podiform chromitites: A case study of high-Cr and high-Al chromitites from Chinese orogenic belts. *Geochim. Cosmochim. Acta* 62, 677–688.
- Zhu, D.C., Pan, G.T., Chung, S.L., Liao, Z.L., Wang, L.Q., Li, G.M., 2008. SHRIMP zircon age and geochemical constraints on the origin of Lower Jurassic volcanic rocks from the Yeba Formation, southern Gangdese, South Tibet. *Int. Geol. Rev.* 50, 442–471.
- Zhu, D., Pan, G., Mo, X., Liao, Z., Jiang, X., Wang, L., Zhao, Z., 2007. Petrogenesis of volcanic rocks in the Sangxiu Formation, central segment of Tethyan Himalaya: A probable example of plume–lithosphere interaction. *J. Asian Earth Sci.* 29, 320–335.
- Zhu, D.C., Zhao, Z.D., Pan, G.T., Lee, H.Y., Kang, Z.Q., Liao, Z.L., Wang, L.Q., Li, G.M., Dong, G.C., Liu, B., 2009. Early cretaceous subduction-related adakite-like rocks of the Gangdese Belt, southern Tibet: products of slab melting and subsequent melt–peridotite interaction? *J. Asian Earth Sci.* 34, 298–309.
- Zindler, A., Hart, S., 1986. Chemical geodynamics. *Earth Planet. Sci. Lett.* 14, 493–571.
- Zyabrev, S.V., Kojima, S., Ahmad, T., 2008. Radiolarian biostratigraphic constraints on the generation of the Nidar ophiolite and the onset of Dras arc volcanism: Tracing the evolution of the closing Tethys along the Indus–Yarlung–Tsangpo suture. *Stratigraphy* 5, 99–112.